

Nonlinear realisation of chiral symmetry breaking in holographic soft wall models

Alfonso Ballon-Bayona^a and Luis A. H. Mamani^b

^a*Instituto de Física, Universidade Federal do Rio de Janeiro,
Caixa Postal 68528, RJ 21941-972, Brazil.*

^b*Centro de Ciências Naturais e Humanas, Universidade Federal do ABC,
Rua Santa Adélia 166, 09210-170, Santo André, SP, Brazil*

E-mail: aballonb@if.ufrj.br, luis.mamani@ufabc.edu.br

ABSTRACT: We investigate nonlinear extensions of the holographic soft wall model proposed by Karch, Katz, Son and Stephanov [1] with a positive quadratic dilaton. We consider a Higgs-like potential for the tachyonic field that brings a more natural realisation of chiral symmetry breaking in the infrared regime. Utilising the AdS/CFT dictionary and holographic renormalisation we find the chiral condensate as a function of the quark mass. The nonlinearity of the Higgs potential leads to a nonlinear relation between the chiral condensate and the quark mass. Solving the effective Schrödinger equations for the field perturbations we estimate meson masses and decay constants and evaluate their dependence on the quark mass. In the axial sector we find an interesting behaviour for the decay constants as the quark mass increases. We also investigate the effect of a 5d running mass for the tachyonic field. We conclude that nonlinear soft wall models with a positive quadratic dilaton do not provide spontaneous symmetry breaking in the chiral limit.

Contents

1	Introduction	1
2	Hard and soft wall models for chiral symmetry breaking	3
2.1	The hard wall model	3
2.2	The (linear) soft wall model	5
3	Nonlinear soft wall models	6
3.1	Asymptotic analysis	7
3.2	Numerical solution	8
3.3	Holographic renormalisation and the chiral condensate	10
3.3.1	Counterterms and covariant subtraction	11
3.3.2	The chiral condensate and the renormalised Hamiltonian	12
3.4	Meson spectrum ($\lambda < 0$)	13
3.4.1	Spectrum of the vector sector	14
3.4.2	Spectrum of the scalar sector	15
3.4.3	Spectrum of the axial-vector sector	16
3.4.4	Spectrum of the pseudoscalar sector	16
3.5	Meson spectrum ($\lambda > 0$)	18
3.5.1	Spectrum of the scalar sector	18
3.5.2	Spectrum of the axial-vector sector	20
3.5.3	Spectrum of the pseudoscalar sector	20
3.6	Decay constants	22
4	Nonlinear soft wall models with running mass	25
4.1	Asymptotic analysis	26
4.2	Numerical solution	27
4.3	Meson Spectrum ($\lambda < 0$)	29
4.3.1	Spectrum of the scalar sector	29
4.3.2	Spectrum of the axial-vector sector	29
4.3.3	Spectrum of the pseudoscalar sector	30
4.4	Meson Spectrum ($\lambda > 0$)	32
4.4.1	Spectrum of the scalar sector	32
4.4.2	Spectrum of the axial-vector sector	32
4.4.3	Spectrum of the pseudoscalar sector	34
4.5	Decay constants	35
5	Discussion and conclusions	37

A	Equations of motion and decay constants	40
B	The GKK model: A review	43
B.1	Scalar sector	44
C	Numerical analysis: nonlinear soft wall model	45

1 Introduction

The dynamical breaking of chiral symmetry in Quantum Chromodynamics (QCD) is a fascinating phenomenon that occurs in the strongly coupled regime. The mechanism for the dynamical generation of quark mass at low energies is crucial for the description of mesons and baryons. The well established order parameter for chiral symmetry breaking is the so called chiral condensate $\langle \bar{q}q \rangle$, which is the VEV of the quark mass operator. A nonzero chiral condensate can be generated by a nontrivial QCD vacuum. Moreover, the phenomenon of chiral symmetry breaking is closely related to the phenomenon of quark confinement [2].

The traditional tools to investigate the nonperturbative regime of QCD are lattice QCD and the Schwinger-Dyson equations. They have provided plenty of insight on the mechanism for dynamical chiral symmetry breaking as well as quantitative predictions for the hadronic phenomenology. More recently, a complementary approach to nonperturbative QCD has been developed. The so called holographic QCD builds 5d gravitational models dual to 4d nonperturbative quantum field theories similar to QCD. This approach is based on the AdS/CFT correspondence and the gauge/gravity duality.

One of the main achievements of the holographic QCD approach is the discovery of a universal criterion for confinement [3]. This was based on the holographic map between 5d classical strings and 4d Wilson loops [4]. The problem of chiral symmetry breaking is also very fascinating in holographic QCD. Since the chiral symmetry group $U(N_f)_L \times U(N_f)_R$ is a 4d global symmetry group, it maps to 5d (local) gauge symmetry group. This implies that 4d chiral symmetry breaking corresponds to a 5d (non-Abelian) gauge symmetry breaking. A minimal 5d holographic QCD model for chiral symmetry breaking was proposed in [5, 6], based on the so called hard wall model [7]. In that approach the 5d gauge symmetry breaking is induced by a 5d tachyonic field X dual to the 4d quark mass operator $\bar{q}q$.

Although the model in [5, 6] successfully introduces the quark mass and chiral condensate, it does not provide a dynamical mechanism for chiral symmetry in the sense that the chiral condensate is fixed by boundary conditions. An alternative approach was proposed in [1], which is known as the soft wall model. That approach

was physically motivated by experimental data on the meson spectrum indicating a set of linear Regge trajectories. In holographic QCD meson masses arise as eigenvalues of effective Schrödinger potentials for 5d field perturbations. The soft wall model introduces a smooth cut off in the form a background scalar field $\Phi(z)$, known as the dilaton. As shown in [1], a positive quadratic dilaton $\Phi(z) \sim z^2$ in the IR leads to approximate linear Regge trajectories for the mesons. Chiral symmetry breaking in the soft wall model is driven by the presence of the dilaton field $\Phi(z)$ and the chiral condensate is not fixed by boundary conditions.

Despite providing a more realistic meson spectrum, the original soft wall model leads to a trivial linear realisation of chiral symmetry breaking driven by an IR regularity condition. Indeed, the chiral condensate $\langle \bar{q}q \rangle$ is just proportional to the quark mass m_q as a consequence of the linearity of the tachyonic field equation. This implies, in particular, that the chiral limit $m_q \rightarrow 0$ in the soft wall model does not lead to spontaneous chiral symmetry breaking because the chiral condensate vanishes. This differs significantly from QCD where spontaneous symmetry breaking always occurs in the chiral limit.

In this work we investigate nonlinear extensions of the holographic soft wall model. We consider a 5d Higgs potential for the tachyonic field X leading to a nonlinear differential equation for the tachyonic field. The nonlinearity also allows us to find a family of solutions in the IR depending in only one parameter, that we call C_0 . For fixed C_0 we will be able to solve numerically the tachyon differential equation. Extracting the source and VEV coefficients for the tachyon solution near the boundary, we utilise the AdS/CFT correspondence and map those parameters to the quark mass and chiral condensate respectively. We will find a nonlinear relation between the chiral condensate $\langle \bar{q}q \rangle$ and the quark mass m_q . We find, in particular, that the chiral condensate always grows with the quark mass, as expected from the perturbative contribution dominant at large m_q , see i.e. [8]. We will find, however, that near the chiral limit $m_q \rightarrow 0$ the nonlinear soft wall models proposed in this work behave in the same way as the original soft wall model and therefore the chiral condensate vanishes. A similar conclusion was recently found in [9].

Our approach was also inspired on the top-down holographic QCD model of [10] where chiral symmetry breaking maps to tachyon condensation in string theory. Our results agree qualitatively with [10] in the regime of large m_q but differ in the chiral limit. We perform a systematic analysis of the background and field perturbations. Our results for the meson spectrum and decay constants support our main conclusions and also bring some surprises. In particular, we find an interesting behaviour for the meson decay constants in the axial sector as functions of the quark mass.

The paper is organised as follows. In section 2 we briefly review chiral symmetry breaking in the hard wall and soft wall models. In section 3 we present the nonlinear extensions of the soft wall model based on a Higgs potential. We perform a systematic analysis of the background including holographic renormalisation for the chiral

condensate. Solving the effective Schrödinger equations for the 5d field perturbations we obtain the meson masses and decay constants. In section 4 we introduce a running mass for the 5d tachyonic field and investigate its effect on the chiral condensate, the meson spectrum and decay constants. We finish the paper in 5 with our conclusions. Appendix A describes the equations for the 5d field perturbations and the dictionary for the meson decay constants. Appendix B briefly reviews the holographic model of [11] whilst appendix C describes some complementary numerical results.

2 Hard and soft wall models for chiral symmetry breaking

Holographic models for QCD at zero temperature satisfy Poincaré invariance. The 5d metric of these models is usually written as

$$ds^2 = e^{2A_s(z)}[-dt^2 + d\vec{x}^2 + dz^2], \quad (2.1)$$

where $A_s(z)$ is the (string-frame) warp-factor as a function of the conformal coordinate z . In this work we are interested in the simplest backgrounds where the 5d metric is just Lorentzian AdS, i.e. $A_s(z) = -\ln z$. Simplifying the background as much as possible allows us to focus on the dynamics of chiral symmetry breaking.

2.1 The hard wall model

In the hard wall model [7] the 5d background is given by

$$ds^2 = \frac{1}{z^2}[-dt^2 + d\vec{x}^2 + dz^2] \quad , \quad 0 < z \leq z_0, \quad (2.2)$$

which corresponds to a 5d Lorentzian AdS space ending in an infrared (IR) hard wall at $z = z_0$. A nice property of the hard wall model is that it satisfies the confinement criterion found in [3]. Soon it was realized that the hard wall model allows us to estimate the spectrum of glueballs [12].

The meson sector of the hard wall model was introduced in [5, 6]. The key ingredients were the 4d quark mass operator $\bar{q}_R q_L$ as well as the left and right 4d currents $J_{(L/R)}^{\mu,a} = \bar{q}_{L/R} \gamma^\mu T^a q_{L/R}$ associated with the chiral symmetry group $SU(N_f)_L \times SU(N_f)_R$. According to the AdS/CFT dictionary the 4d quark mass operator maps to a 5d scalar X field with mass given by the relation $m_X^2 = \Delta(\Delta - 4)$ with Δ the conformal dimension of the quark mass operator. In the extreme ultraviolet (UV) we have $\Delta = 3$ and this corresponds to $m_X^2 = -3$. This 5d mass would indicate an instability in Minkowski space and therefore the 5d field X is usually called the tachyon. The left and right 4d currents, on the other hand, are conserved in the extreme UV so they are mapped to 5d gauge fields $A_{L/R}^{\mu,a}$.

In QCD chiral symmetry is broken dynamically in the IR due to a nontrivial vacuum and the dynamics of the quark mass operator. An important observable

is the so called chiral condensate σ , which is the VEV of the quark mass operator, i.e. $\sigma = \langle \bar{q}q \rangle$. The authors in [5, 6] realised that chiral symmetry breaking in 4d corresponds to 5d gauge symmetry breaking of the fields $A_{L/R}^{\mu,a}$ driven by a nontrivial scalar field X . In this work we use the conventions of [5] and write the 5d action as

$$S = - \int d^5x \sqrt{-g} \text{Tr} \left[|D_m X|^2 + m_X^2 |X|^2 + \frac{1}{g_5^2} F_{mn}^{(L)^2} + \frac{1}{4g_5^2} F_{mn}^{(R)^2} \right], \quad (2.3)$$

where

$$\begin{aligned} F_{mn}^{(L/R)} &= \partial_m A_n^{(L/R)} - \partial_n A_m^{(L/R)} - i[A_m^{(L/R)}, A_n^{(L/R)}], \\ D_m X &= \partial_m X - iA_m^{(L)} X + iX A_m^{(R)}. \end{aligned} \quad (2.4)$$

Note that under the gauge group $SU(N_f)_L \times SU(N_f)_R$ the left and right vector fields $A_m^{(L/R)}$ transform as adjoint fields whereas the scalar field X behaves as a bifundamental. For now on we take $N_f = 2$ and make the assumption of isospin (flavor) symmetry, i.e. $m_u = m_d$ and $\sigma_u = \sigma_d$, which is a good approximation for the light quark sector in QCD. Therefore we take the following ansatz for the 5d tachyonic field:

$$X(z) = \frac{1}{2} v(z) I_{2 \times 2}. \quad (2.5)$$

In QCD at zero temperature (and zero density) we do not expect any vectorial condensate so we take the following ansatz for the 5d gauge fields

$$A_m^{L/R} = 0. \quad (2.6)$$

The 5d action in (2.3) reduces to a 1d action for the field $v(z)$ and the Euler-Lagrange equation takes the form

$$\left[(z\partial_z)^2 - 4z\partial_z - m_X^2 \right] v = 0, \quad (2.7)$$

with exact solution

$$v(z) = c_1 z^{\Delta_-} + c_3 z^{\Delta_+}, \quad \Delta_{\pm} = 2 \pm \sqrt{4 + m_X^2}. \quad (2.8)$$

This has the expected scaling behaviour for a 5d scalar field dual to an operator of dimension Δ_+ with coupling of dimension $\Delta_- = 4 - \Delta_+$. In order to match to the quark mass operator in the extreme UV we choose $\Delta_+ = 3$. The source coefficient c_1 is related to the quark mass m_q by $c_1 = m_q \zeta$ where ζ is a normalization constant. This constant is usually fixed as $\zeta = \sqrt{N_c}/2\pi$ to be consistent with counting rules of large- N_c QCD [13]. The VEV coefficient c_3 will be related to the quark condensate σ_u . The precise relation is scheme-dependent and will be obtained in the next section.

In the hard wall model the VEV coefficient c_3 is fixed by boundary conditions at the IR wall $z = z_0$. This differs from what we expect in QCD where the chiral condensate is generated dynamically due to a nontrivial vacuum and confinement. The hard wall model, however, has the nice feature of being the simplest model that describes at the same time confinement and chiral symmetry breaking.

2.2 The (linear) soft wall model

A shortcoming of the hard wall model is that it leads to hadronic masses that grow too fast as we increase the radial number. For example, the resonances of the ρ meson have masses that grow as $m_{\rho(n)}^2 \sim n^2$ for large n . Experimental data, on the other hand, indicates an approximate linear dependence for the squared masses, i.e. $m_{\rho(n)}^2 \sim n$.

The quadratic dependence in the hard wall model can be thought as a consequence of having a metric that abruptly ends at a cutoff $z = z_0$. Motivated by this problem, the authors of [1] proposed the idea of a smooth cutoff driven by a background scalar field $\Phi(z)$ where the geometry does not abruptly end. This was inspired by string theory where the field Φ is known as the dilaton. Later works have explored the backreaction of this background field on the AdS metric and the map to the Yang-Mills operator $\text{Tr} F^2$ [14–16].

In the soft wall model the background is given by

$$ds^2 = \frac{1}{z^2}[-dt^2 + d\vec{x}^2 + dz^2] \quad , \quad \Phi(z) = \phi_\infty z^2, \quad (2.9)$$

and the flavor sector is described by the action

$$S = - \int d^5x \sqrt{-g} e^{-\Phi(z)} \text{Tr} \left[|D_m X|^2 + m_X^2 |X|^2 + \frac{1}{g_5^2} F_{mn}^{(L)2} + \frac{1}{4g_5^2} F_{mn}^{(R)2} \right], \quad (2.10)$$

The quadratic dependence of $\Phi(z)$ leads to a harmonic oscillator form of the effective Schrödinger potential at large z for the field perturbations. This guarantees the linear dependence for the squared masses of mesons.

For the background fields we take the ansatz (2.5)-(2.6) and this time we find the equation

$$\left[z^2 \partial_z^2 - (3 + 2\phi_\infty z^2) z \partial_z - m_X^2 \right] v = 0. \quad (2.11)$$

In order to find an exact solution we rewrite (2.11) in terms of a new variable $x \equiv \phi_\infty z^2$ and redefine the field $v(x)$ as $x^\beta \tilde{v}(x)$. We arrive at the 2nd order differential equation

$$\left\{ x^2 \partial_x^2 + [2\beta - 1 - x] x \partial_x + \beta^2 - 2\beta - \frac{m_X^2}{4} - \beta x \right\} \tilde{v} = 0. \quad (2.12)$$

This equation becomes Kummer's equation if

$$\beta^2 - 2\beta - \frac{m_X^2}{4} = 0 \quad \rightarrow \quad \beta = 1 \pm \sqrt{1 + \frac{m_X^2}{4}} = \frac{\Delta_\pm}{2}. \quad (2.13)$$

The solutions for $\tilde{v}(z)$ are of the form $M(\beta, 2\beta - 1; x)$ (Kummer) and $U(\beta, 2\beta - 1; x)$ (Tricomi). From this analysis we conclude that the exact solution for $v(z)$ can be written as

$$v(z) = \tilde{c}_1 z^{\Delta_-} U\left(\frac{\Delta_-}{2}, \Delta_- - 1; \phi_\infty z^2\right) + \tilde{c}_3 z^{\Delta_+} M\left(\frac{\Delta_+}{2}, \Delta_+ - 1; \phi_\infty z^2\right). \quad (2.14)$$

For $m_X^2 = -3$ we have $\Delta_- = 1$ and $\Delta_+ = 3$. This solution was first obtained in [17]. Noticing that when $x \rightarrow \infty$ we have $M(a, b; x) \sim e^x x^{a-b}$ and $U(a, b; x) \sim x^{-a}$ we see that we need to set $\tilde{c}_3 = 0$ in order to avoid a divergent solution in the IR. The tachyon solution in (2.14) becomes

$$v(z) = \frac{\sqrt{\pi}}{2} c_1 z U\left(\frac{1}{2}, 0; \phi_\infty z^2\right), \quad (2.15)$$

where \tilde{c}_1 was rewritten as $\sqrt{\pi}/2 c_1$. In the UV (small z), the solution in (2.15) behaves as

$$v^{UV}(z) = c_1 z + d_3(c_1) \ln z + c_3(c_1) z^3 + \dots \quad (2.16)$$

The logarithmic term could have been anticipated from a Frobenius method. Both coefficients d_3 and c_3 are actually proportional to c_1 and then vanish in the chiral limit $c_1 \rightarrow 0$. In the IR the tachyon solution (2.15) behaves as

$$v^{IR}(z) = C_0 \left[1 + \mathcal{O}(z^{-2})\right], \quad C_0 = \frac{\sqrt{\pi}}{2} \frac{c_1}{\sqrt{\phi_\infty}}. \quad (2.17)$$

The parameter C_0 characterises the tachyon solution at large z . As expected, the solution is regular in the IR. This regular solution was, however, chosen by setting $\tilde{c}_3 = 0$. In the next section we will introduce a nonlinear potential for the tachyonic field. The nonlinearity of the new differential equation will naturally lead to regular solutions in the IR without the need of fixing any integration constant.

3 Nonlinear soft wall models

The authors in [1] realised that the trivial linear dependence of c_3 on c_1 differed significantly from what one expects in QCD for the chiral condensate σ_q as a function of the quark mass m_q . They suggested that the model could be improved by adding nonlinear terms to the tachyonic potential. The nonlinearity would lead to solutions in the IR characterised by only one parameter, C_0 , and the relation between the IR parameter C_0 and the UV parameter c_1 would also be nonlinear.

In this work we investigate a nonlinear potential of the Higgs form

$$U(|X|) = m_X^2 |X|^2 + \lambda |X|^4. \quad (3.1)$$

This time the 5d action for the flavor sector becomes

$$S = - \int d^5x \sqrt{-g} e^{-\Phi(z)} \text{Tr} \left[|D_m X|^2 + m_X^2 |X|^2 + \lambda |X|^4 + \frac{1}{g_5^2} F_{mn}^{(L)2} + \frac{1}{4g_5^2} F_{mn}^{(R)2} \right]. \quad (3.2)$$

We will consider both cases $\lambda < 0$ and $\lambda > 0$ and also recover the original soft wall model when $\lambda \rightarrow 0$. As in the previous cases, we take $m_X^2 = -3$ for the tachyonic field.

For the background fields we take again the ansatz (2.5)-(2.6). This time we obtain a nonlinear equation for the tachyon:

$$\left[z^2 \partial_z^2 - (3 + 2\phi_\infty z^2) z \partial_z + 3 \right] v - \frac{\lambda}{2} v^3 = 0. \quad (3.3)$$

This time we can not obtain an analytic solution. Below we describe the asymptotic solutions for the tachyon in the UV and IR regimes and present our numerical results for the tachyon profiles.

3.1 Asymptotic analysis

In the UV we consider the Frobenius ansatz

$$v(z) = c_1 z + d_3 z^3 \ln z + c_3 z^3 + d_5 z^5 \ln z + c_5 z^2 + \dots \quad (3.4)$$

Plugging this ansatz into the tachyon equation (3.3) we find the UV coefficients

$$\begin{aligned} d_3 &= \frac{1}{4} c_1 (c_1^2 \lambda + 4\phi_\infty) \quad , \quad d_5 = \frac{3}{64} c_1 (c_1^2 \lambda + 4\phi_\infty)^2 + , \\ c_5 &= \frac{1}{256} (c_1^2 \lambda + 4\phi_\infty) (-9c_1^3 \lambda - 20c_1 \phi_\infty + 48c_3) \quad , \quad \dots \end{aligned} \quad (3.5)$$

Note that d_3 and d_5 depend only on c_1 whereas c_5 depends on c_1 and c_3 . In the special case $c_1^2 \lambda + 4\phi_\infty = 0$ all the subleading terms vanish and the linear solution $v(z) = c_1 z$ becomes exact. This is only possible for $\lambda < 0$ because in the soft wall model we have $\phi_\infty > 0$.

The VEV parameter c_3 appears to be independent of c_1 . We will see, however, that in the IR the tachyon solution is characterised by a single parameter C_0 . The UV parameters c_1 and c_3 then can be thought as functions of the IR parameter C_0 . As a consequence c_3 will depend on c_1 in nonlinear fashion, as predicted in [1]. As far as we are concerned, the first realisation of this tachyon dynamics was developed in the top-down holographic QCD model of [10].

In the IR it is convenient to work with the variable $y = 1/z$. Thus, the differential equation (3.3) may be written as

$$\left[(y \partial_y)^2 + 2 (2 + \phi_\infty y^{-2}) (y \partial_y) + 3 \right] v - \frac{\lambda}{2} v^3 = 0. \quad (3.6)$$

We first consider the power ansatz

$$v^{IR}(y) = C_0 y^\alpha. \quad (3.7)$$

Plugging this ansatz into (3.1) we obtain the polynomial equation

$$C_0 y^\alpha (\alpha^2 + 4\alpha + 3) + C_0 y^{\alpha-2} (2\alpha\phi_\infty) - \frac{\lambda}{2} C_0^3 y^{3\alpha} = 0. \quad (3.8)$$

The first term in (3.8) is subleading compared to the second. The third term compete with the second term only when $\alpha < 0$. We distinguish 3 cases: $\alpha > -1$, $\alpha = -1$ and $\alpha < -1$. The latter case is trivial because it leads to $C_0 = 0$.

In the case $\alpha > -1$ the second term always dominate and we find $\alpha = 0$. This is the regular solution we were looking for and admits the following expansion

$$v^{IR}(y) = C_0 + C_2 y^2 + C_4 y^4 + \dots, \quad (3.9)$$

with the subleading IR coefficients given by

$$C_2 = \frac{C_0}{8\phi_\infty}(C_0^2\lambda - 6) \quad , \quad C_4 = \frac{3C_0}{128\phi_\infty^2}(C_0^2\lambda - 6)(C_0^2\lambda - 10). \quad (3.10)$$

To guarantee the convergence of the series (3.9) we need a condition of the form $|C_0^2\lambda|/\phi_\infty < 1$. In the special case $C_0^2\lambda - 6 = 0$ all the subleading coefficients vanish and the constant solution is exact. This can only be obtained in the case $\lambda > 0$ and, interestingly, it corresponds to the minimum of the Higgs potential $\partial_v U = 0$.

In the special case $\alpha = -1$ we see in (3.8) that the first term vanishes whereas the second and third terms are of order y^{-3} leading to the condition $C_0^2\lambda + 4\phi_\infty = 0$. This divergent solution is linear, i.e. $v(z) = C_0 z$ and it is valid only for $\lambda < 0$. This linear solution appears to be exact and it may be related to previous approaches to nonlinear soft wall models, such as [11]. The model of [11] is briefly discussed in appendix B.

3.2 Numerical solution

Once the asymptotic analysis has been done, we can proceed to integrate numerically the nonlinear differential equation for the tachyon field (3.3). We may integrate (3.3) from the UV to the IR using the UV asymptotic solution (3.4) to extract initial conditions. By matching the numerical solution to the IR analytic solution (3.9) we find a relation between the UV parameters c_1 and c_3 as well as the corresponding IR parameter C_0 . Alternatively, we can integrate numerically (3.3) from the IR to the UV using the IR analytic solution (3.9) and this time the matching procedure allows us to extract the UV parameters c_1 and c_3 in terms of the IR parameter C_0 .

We show in Fig. 1 typical profiles for the tachyon field $v(z)$ for fixed C_0 and different values of λ . The linear soft wall model, corresponding to $\lambda = 0$, is depicted by the black dotted line and we see that the effect of a nonlinear negative (positive) quartic coupling λ is to deform the tachyon profile to the right (left). In the case of $\lambda > 0$ we have an upper bound $C_0^2\lambda < 6$ for the tachyon solution. As we approach that bound the tachyon profile becomes constant in z , which is consistent with the asymptotic analysis done in the previous subsection.

Our numerical results for the UV parameters c_1 and c_3 as functions of the IR parameter C_0 are displayed in Fig. 2 for different values of λ . The linear soft wall model

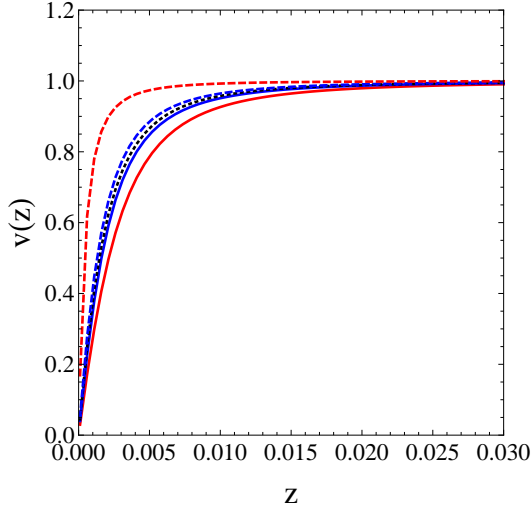


Figure 1. Tachyon profiles for $C_0 = 1$ and λ varying from -5 (red solid) to 5 (red dashed). The black dotted profile in the middle corresponds to $\lambda = 0$ (linear soft wall model).

($\lambda = 0$) is represented by the black dotted line. All solutions enjoy the symmetry $(c_1, c_3) \leftrightarrow (-c_1, -c_3)$, present in the differential equation (3.3). The physical regime, of course, corresponds to $c_1 > 0$. We see that the nonlinearity of the tachyon differential equation leads to nonlinear relations $c_1(C_0)$ and $c_3(C_0)$, as expected. However, in the chiral limit (corresponding to $c_1 \rightarrow 0$) all parameters go to zero. In particular, the VEV parameter c_3 (associated with the 4d chiral condensate) vanishes. This differs significantly from QCD where chiral symmetry is spontaneously broken in the chiral limit leading to a nonzero chiral condensate. Note that nonlinearity brings saturation effects. In the case $\lambda > 0$ there is an upper bound for C_0 (described in the previous paragraph) whereas in the case $\lambda < 0$ we have an upper bound in c_1 . The upper bound in c_1 would imply a cutoff for the quark mass, which is not expected in QCD.

In Fig 3 we show the VEV parameter c_3 as a function of the source parameter c_1 in the physical regime. This result will be interpreted in terms of the 4d chiral condensate $\langle \bar{q}q \rangle$ as a function of the quark mass m_q , as described in the next subsection. The linear relation $c_3 \sim c_1$, characteristic of the linear soft wall model, is a good approximation at small c_1 . For positive λ the VEV parameter c_3 grows monotonically with c_1 , which is the expected behaviour for $\langle \bar{q}q \rangle$. A similar behaviour was obtained in the top-down holographic QCD model developed in [10]. The case of negative λ leads to a non-monotonic function $c_3(c_1)$. In that case the VEV parameter c_3 vanishes when c_1 reaches its upper bound. We conclude that the case $\lambda > 0$ leads to the more realistic scenario. This could have been anticipated by the fact that $\lambda > 0$ in (3.1) corresponds to the Mexican hat potential for the Higgs field.

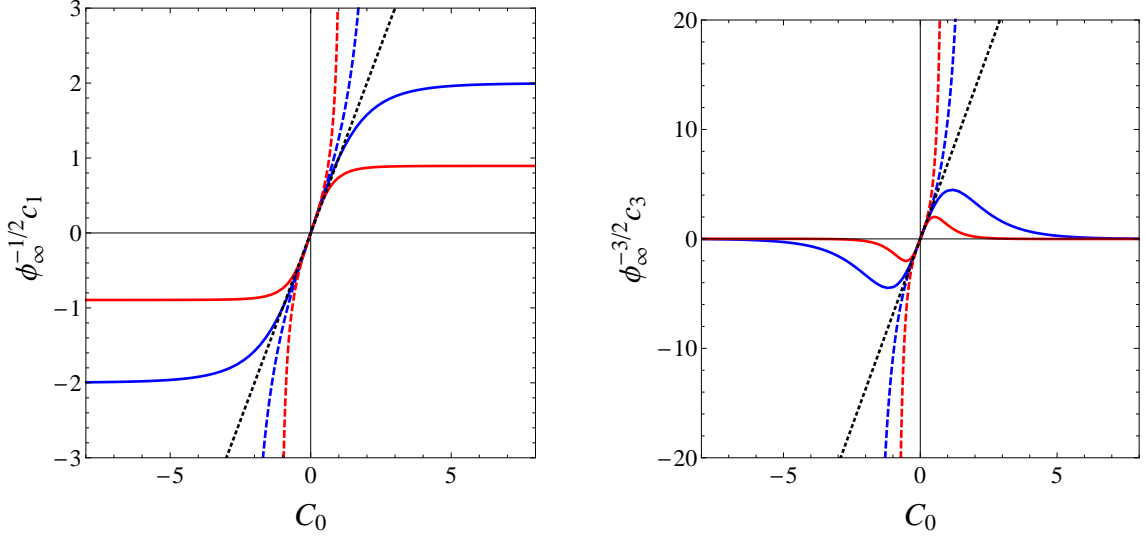


Figure 2. Numerical results for c_1 (left panel) and c_3 (right panel) as functions of C_0 in units of $\sqrt{\phi_\infty}$. The blue and red solid lines (dashed lines) correspond to $\lambda = -1$ and $\lambda = -5$ ($\lambda = 1$ and $\lambda = 5$). The black dotted line corresponds to $\lambda = 0$.

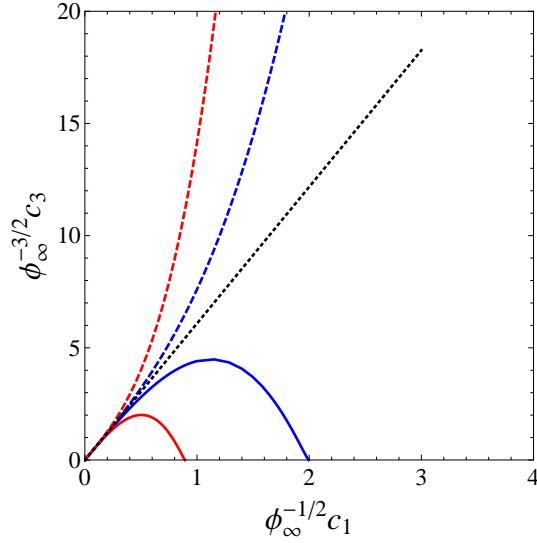


Figure 3. The VEV parameter c_3 as a function of the source parameter c_1 , in units of $\sqrt{\phi_\infty}$, for different values of λ . The blue and red solid lines (dashed lines) correspond to $\lambda = -1$ and $\lambda = -5$ ($\lambda = 1$ and $\lambda = 5$). The black dotted line corresponds to $\lambda = 0$.

3.3 Holographic renormalisation and the chiral condensate

In this subsection we describe the procedure of holographic renormalisation for the nonlinear soft wall models proposed in this work. The case at hand is similar to the case of probe branes in a fixed background, see e.g. [10, 18]. The starting point is the on-shell action. For the background tachyonic field the action in (3.2) becomes

on-shell

$$S_{\text{os}} = S_{\text{Bdy}} + S_{\text{Int}} , \quad (3.11)$$

where

$$S_{\text{Bdy}} = -\frac{1}{2} \int d^4x \Pi_z(z_0) v(z_0) \quad , \quad \Pi_z = -z^{-3} e^{-\Phi(z)} \partial_z v , \quad (3.12)$$

$$S_{\text{Int}} = \frac{\lambda}{8} \int d^4x dz z^{-5} e^{-\Phi(z)} v^4 . \quad (3.13)$$

S_{Bdy} is a boundary term (the AdS boundary is located at $z_0 \ll 1$) and $\Pi_z = \partial \mathcal{L} / \partial(\partial_z v)$ is the conjugate momentum in z . The bulk term S_{Int} appears because of the nonlinear term in the tachyon potential.

3.3.1 Counterterms and covariant subtraction

Plugging the UV asymptotic solution (3.4) into the surface term (3.12) we see that it splits into divergent and finite pieces

$$S_{\text{Bdy}} = S_{\text{Bdy}}^{\text{Div}} + S_{\text{Bdy}}^{\text{Fin}} , \quad (3.14)$$

$$S_{\text{Bdy}}^{\text{Div}} = \frac{1}{2} \int d^4x \left[c_1^2 z_0^{-2} + c_1^2 (c_1^2 \lambda + 4\phi_\infty) \ln z_0 \right] , \quad (3.15)$$

$$S_{\text{Bdy}}^{\text{Fin}} = \frac{1}{2} \int d^4x \left[\frac{1}{4} c_1^4 \lambda + 4c_1 c_3 \right] . \quad (3.16)$$

We have omitted in (3.16) the terms that vanish in the limit $z_0 \rightarrow 0$. The bulk term (3.13) can not be split in a simple way but from (3.4) we find the divergent piece

$$S_{\text{Int}}^{\text{Div}} = -\frac{\lambda}{8} \int d^4x c_1^2 \ln z_0 , \quad (3.17)$$

and simply define the finite piece as

$$S_{\text{Int}}^{\text{Fin}} = S_{\text{Int}} - S_{\text{Int}}^{\text{Div}} . \quad (3.18)$$

In order to cancel the UV divergences (3.15)-(3.17) in a consistent way we introduce the covariant counterterms

$$\begin{aligned} S_{\text{ct}} = & - \int d^4x \sqrt{-\gamma} \left\{ a_1 v^2(z_0) + \ln z_0 \left[a_2 \Phi(z_0) v^2(z_0) - a_3 \lambda v^4(z_0) \right] \right. \\ & \left. + a_4 v^2(z_0) \Phi(z_0) - a_5 \lambda v^4(z_0) \right\} . \end{aligned} \quad (3.19)$$

The first three terms in (3.19) are the minimal required to cancel the UV divergences. The last two terms in (3.19) are finite counterterms associated with the renormalisation scheme dependence of the 4d dual theory. The action in (3.19) can be split

into divergent and finite pieces

$$S_{\text{ct}} = S_{\text{ct}}^{\text{Div}} + S_{\text{ct}}^{\text{Fin}}, \quad (3.20)$$

$$S_{\text{ct}}^{\text{Div}} = - \int d^4x \left\{ a_1 c_1^2 z_0^{-2} + \left[(2a_1 + a_2) c_1^2 \phi_\infty + \left(\frac{a_1}{2} - a_3 \right) c_1^4 \lambda \right] \ln z_0 \right\}, \quad (3.21)$$

$$S_{\text{ct}}^{\text{Fin}} = - \int d^4x \left[2a_1 c_1 c_3 + a_4 c_1^2 \phi_\infty - a_5 c_1^4 \lambda \right]. \quad (3.22)$$

The renormalised action is then defined as

$$S_{\text{Ren}} = S_{\text{Bdy}} + S_{\text{Int}} + S_{\text{ct}}. \quad (3.23)$$

The UV divergences cancel for

$$a_1 = \frac{1}{2}, \quad a_2 = 1, \quad a_3 = -\frac{1}{8}, \quad (3.24)$$

and the renormalised action takes the form

$$S_{\text{Ren}} = S_{\text{Bdy}}^{\text{Fin}} + S_{\text{Int}}^{\text{Fin}} + S_{\text{ct}}^{\text{Fin}}. \quad (3.25)$$

3.3.2 The chiral condensate and the renormalised Hamiltonian

The CFT deformation due to the quark mass operator has the form $\int d^4x m_q \langle \bar{q}q \rangle$. Therefore the dictionary for the chiral condensate takes the form

$$\langle \bar{q}q \rangle = \zeta \left[\frac{\delta S_{\text{os}}}{\delta c_1} + \frac{\delta S_{\text{ct}}}{\delta c_1} \right], \quad (3.26)$$

where

$$\begin{aligned} \frac{\delta S_{\text{os}}}{\delta c_1} &= - \frac{\partial v(z_0)}{c_1} \Pi_z(z_0) \\ &= c_1 z_0^{-2} + \left(4c_1 \phi_\infty - \frac{3}{2} c_1^3 \lambda \right) \ln z_0 + 3c_3 + c_1 \partial_{c_1} c_3 + \frac{1}{4} c_1^3 \lambda, \end{aligned} \quad (3.27)$$

is the bare contribution and

$$\frac{\delta S_{\text{ct}}}{\delta c_1} = -c_1 z_0^{-2} - \left(4c_1 \phi_\infty + \frac{3}{2} c_1^3 \lambda \right) \ln z_0 - c_3 - c_1 \partial_{c_1} c_3 - 2a_4 c_1 \phi_\infty + 4a_5 c_1^3 \lambda, \quad (3.28)$$

is the counterterms contribution. From (3.26), (3.27) and (3.28) we see that the UV divergences cancel and we arrive at the final expression for the chiral condensate

$$\langle \bar{q}q \rangle = \zeta \left[2c_3 - 2a_4 c_1 \phi_\infty + \frac{1}{4} c_1^3 \lambda (1 + 16a_5) \right]. \quad (3.29)$$

The coefficients a_4 and a_5 reflect the scheme dependence on the chiral condensate. Since we already know that c_3 has a very similar behaviour to the QCD chiral condensate in the nonperturbative regime we suspect that the natural choice for fixing

the scheme would be $a_4 = 0$ and $a_5 = -1/16$. In figure 4 we plot the renormalised Hamiltonian and the chiral condensate, in units $\sqrt{\phi_\infty}$, for that particular scheme. As promised, we find a nonlinear relation between the chiral condensate and the quark mass. As described in the previous subsection, the model with $\lambda > 0$ provides a more realistic description of the chiral condensate. It can be checked that the chiral condensate could have been obtained directly by the relation $\langle \bar{q}q \rangle = -\partial H^{Ren}/\partial m_q$.

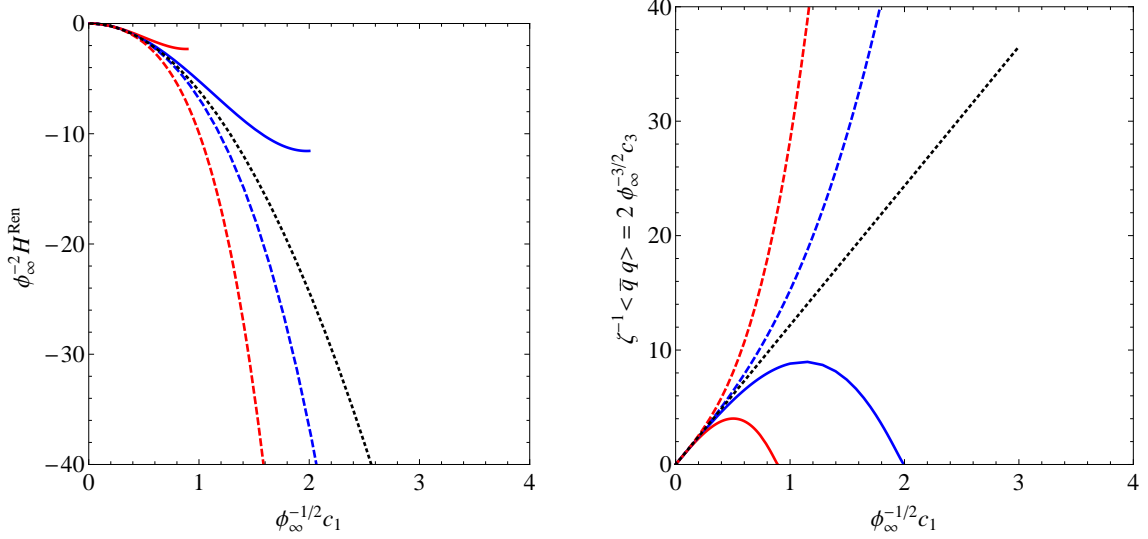


Figure 4. Left (right) panel: The renormalised Hamiltonian (chiral condensate) as a function of the quark mass parameter c_1 in units $\sqrt{\phi_\infty}$. The scheme was fixed setting $a_4 = 0$ and $a_5 = -1/16$. The blue and red solid (dashed) lines correspond to $\lambda = -1$ and $\lambda = -5$ ($\lambda = 1$ and $\lambda = 5$) respectively. The black dotted line corresponds to $\lambda = 0$ (linear case).

3.4 Meson spectrum ($\lambda < 0$)

The non-Abelian Higgs action in (3.2) describes the dynamics of the scalar tachyonic field X as well as the left and right gauge fields $A_m^{(L/R)}$. At the beginning of this section we analysed the background tachyonic field $X = \frac{1}{2}v(z)$ (the background gauge fields were set to zero). Now we consider the perturbations of X and $A_m^{(L/R)}$. As described in appendix A, the perturbations associated with the tachyonic field are the scalar field S and the pseudoscalar fields π^a . The former will describe a tower of scalar mesons whereas the latter will be related to the pseudoscalar mesons (pions for $N_f = 2$). On the other hand, the gauge field fluctuations will be written as $A_m^{(L/R)} = V_m \pm A_m$ with $v_m = V_m^a T^a$ and $A_m = A_m^a T^a$.

As described in appendix A, the vector field V_m^a decompose as (V_z^a, V_μ^a) and V_μ^a will describe a tower of 4d vector mesons. The axial-vector field A_m^a decompose as (A_z^a, A_μ^a) and in turn A_μ^a decompose into transverse $A_m^{\perp,a}$ and longitudinal parts

$\partial_\mu \phi^a$. The fields $A_m^{\perp,a}$ will describe a tower of axial-vector mesons whereas the fields ϕ^a couple to the fields π^a to describe the tower of pseudoscalar mesons. The equations for the vector sector $V_m^{\perp,a}$, scalar sector S , axial-vector sector $A_m^{\perp,a}$ and pseudoscalar sector (π^a, ϕ^a) are obtained from a second order expansion of the action (3.2), as described in appendix A.

3.4.1 Spectrum of the vector sector

We start with the equation of motion (A.9) (the flavor index is hidden in the following analysis). After performing the Fourier transform $V_\mu(x^\mu, z) \rightarrow V_\mu(k^\mu, z)$ on (A.9), where we have set $\square \rightarrow m_V^2$, the equation may be written in the Schrödinger form through the transformation $V_n = e^{-B_V} \psi_{v_n}$, where $B_V = (A_s - \Phi)/2$. The effective Schrödinger equation reads

$$[-\partial_z^2 + V_V] \psi_{v_n} = m_V^2 \psi_{v_n}, \quad (3.30)$$

where the potential is given by

$$V_V = (\partial_z B_V)^2 + \partial_z^2 B_V. \quad (3.31)$$

In this case the problem has an exact solution [1]

$$m_V^2 = 4\phi_\infty(1+n), \quad n = 0, 1, 2, \dots \quad (3.32)$$

At this point the free parameter is ϕ_∞ , we may fix the value of this parameter by comparing the first vector state with the corresponding experimental value of the ρ meson, as was done in e.g. Ref. [19]. Thus, the value is $\phi_\infty = (388 \text{ MeV})^2$.

The spectrum obtained is shown in Table 1, labelled as SW, compared against the holographic model of [11] and experimental data [20]. The details of [11] are given in appendix B.

n	SW [1]	GKK [11]	ρ experimental [20]
1	776	475	776 ± 1
2	1097	1129	1282 ± 37
3	1344	1429	1465 ± 25
4	1552	1674	1720 ± 20
5	1735	1884	1909 ± 30
6	1901	2072	2149 ± 17
7	2053	2243	2265 ± 40

Table 1. The mass of the vector mesons (in MeV) obtained in the the soft wall model, compared against the holographic model [11] and experimental results of PDG [20].

3.4.2 Spectrum of the scalar sector

Now, we proceed to calculate the spectrum of the scalar mesons. This sector is obtained from the fluctuations of the tachyon field, cf. Eq. (A.1), where $S(x, z)$ represents the scalar field related to the scalar mesons. After performing the Fourier transform $S(x^\mu, z) \rightarrow S(k^\mu, z)$ on (A.11), where we have set $\square \rightarrow m_s^2$ and , we arrive at the following equation

$$e^{-3A_s+\Phi}\partial_z\left(e^{3A_s-\Phi}\partial_z S(k, z)\right) + m_s^2 S(k, z) - e^{2A_s}\left(m_X^2(z) + \frac{3}{2}\lambda v^2(z)\right) S(k, z) = 0, \quad (3.33)$$

where $m_X^2(z) = -3$. We rewrite the last equation in a Schrödinger form, redefining the scalar modes as $S_n = e^{-B_S}\psi_{s_n}(z)$, where $B_S = 3A_s/2 - \Phi/2$. Thus, we get

$$-\partial_z^2 \psi_{s_n} + V_S \psi_{s_n} = m_s^2 \psi_{s_n}, \quad (3.34)$$

with the Schrödinger potential given by

$$V_S = (\partial_z B_S)^2 + \partial_z^2 B_S + e^{2A_s}\left(m_X^2 - \frac{3\lambda}{2}v^2(z)\right). \quad (3.35)$$

For $\lambda = 0$ the potential (3.35) reduces to the one obtained in Ref. [17]. Notice that the parameter λ controls the minimum value of the potential (3.35) as shown in Fig. 5. For $\lambda < 0$, the potential allows us to describe lightest states. This statement is supported by the results displayed in Fig. 6, where we can see the evolution of the meson with the parameter C_0 (left panel) and c_1 (right panel). Those results were obtained for $\lambda = -2$ (solid lines) and $\lambda = 0$ (dashed lines).

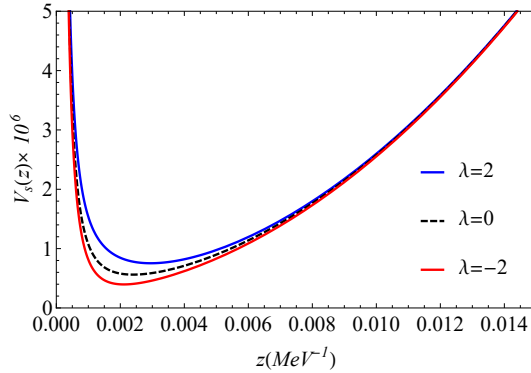


Figure 5. The potential of the Schrödinger equation for $\phi_\infty = (388 \text{ MeV})^2$ and three different values of the parameter λ .

These results indicate the possibility of fixing the parameter C_0 , for given λ , requiring the first eigenvalue of the Schrödinger equation to match the mass of the scalar meson $f_0(550 \text{ MeV})$. However, the status of the $f_0(550 \text{ MeV})$ as a scalar meson is not established. We follow a more conservative approach and consider $f_0(980 \text{ MeV})$ as

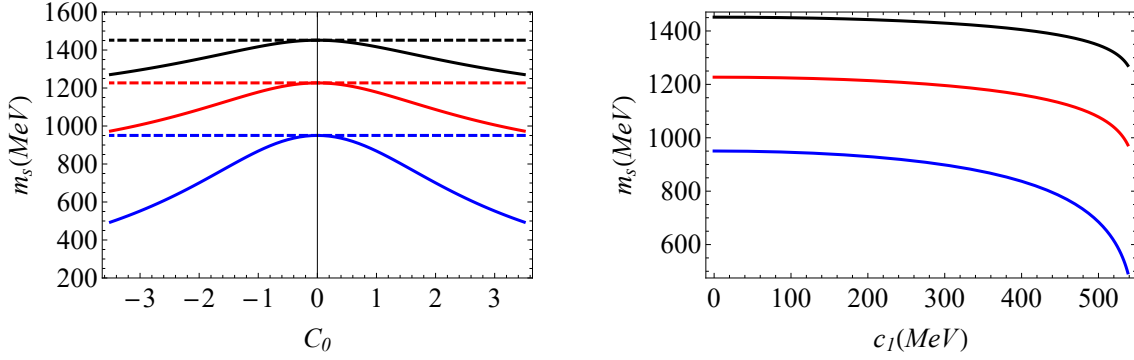


Figure 6. The mass of the scalar mesons as a function of C_0 (left) and c_1 (right). Solid lines represent the results for $\lambda = -2$, while dashed lines for $\lambda = 0$. The results were obtained setting $\phi_\infty = (388 \text{ MeV})^2$.

the first scalar meson, as in Ref. [21]. As the upper limit for the scalar mass in our model is the one obtained for $\lambda = 0$, $m_s = 950 \text{ (MeV)}$, see Fig. 6, it is not possible to reach the state $f_0(980 \text{ MeV})$ when $\lambda < 0$.

It is worth mentioning that the behaviour of the scalar meson mass as a function of the quark mass, i.e., c_1 , displayed in Fig. 6 is opposite to the one expected in QCD. Hence, the model with $\lambda < 0$ is pathologic in the scalar sector.

3.4.3 Spectrum of the axial-vector sector

After performing the Fourier transform $A_\perp^\mu(x^\mu, z) \rightarrow A_\perp^\mu(k^\mu, z)$ on (A.13), with $\square \rightarrow m_A^2$ and, redefining the axial-vector mode as $a_n(z) = e^{-B_A} \psi_{a_n}(z)$, where $B_A = (A_s - \Phi)/2$, we arrive at the equation

$$-\partial_z^2 \psi_{a_n} + V_A \psi_{a_n} = m_A^2 \psi_{a_n}, \quad (3.36)$$

with the Schrödinger potential given by

$$V_A = (\partial_z B_A)^2 + \partial_z^2 B_A + g_5^2 e^{2A_s} v^2(z). \quad (3.37)$$

The left panel of Fig. 7 shows our results for the masses of the axial-vector states as a function of the parameter C_0 , compared against the corresponding values in the linear soft wall model, i.e., $\lambda = 0$. The right panel of the figure shows how the masses dependence on the parameter the quark mass parameter c_1 . In this case the masses increase with c_1 , which is the expected behaviour for mesons.

These results suggest the possibility of using the mass of the first axial-vector meson $a_1(1230)$ to fix the parameter C_0 for given λ .

3.4.4 Spectrum of the pseudoscalar sector

The pseudoscalar sector is special because it is described by a coupled system of differential equations (A.14)- (A.15). After performing the Fourier transform $\pi(x^\mu, z) \rightarrow$

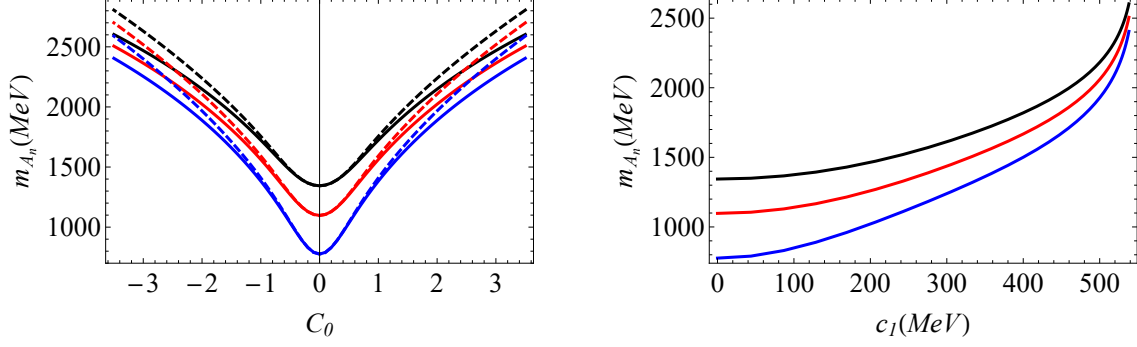


Figure 7. Masses of axial-vector mesons as functions of C_0 (left) and c_1 (right). Solid lines represent the results for $\lambda = -2$, while dashed lines for $\lambda = 0$. The results were obtained setting $\phi_\infty = (388 \text{ MeV})^2$.

$\pi(k^\mu, z)$ and $\varphi(x^\mu, z) \rightarrow \varphi(k^\mu, z)$ in both equations, where we have set $\square \rightarrow m_\pi^2$, we get the following equations

$$e^{-A_s+\Phi} \partial_z (e^{A_s-\Phi} \partial_z \varphi) + g_5^2 e^{2A_s+2\log v} (\pi - \varphi) = 0, \quad (3.38)$$

$$-m_\pi^2 \partial_z \varphi + g_5^2 e^{2A_s+2\log v} \partial_z \pi = 0. \quad (3.39)$$

We follow [22] and decouple this system of equations. The decoupled equation is second order in the auxiliary field $\Pi = \partial_z \pi_n$ and takes the form

$$-\partial_z^2 \Pi + \partial_z (\Phi - A_s - \ln \beta) \partial_z \Pi + (\partial_z^2 (\Phi - A_s - \ln \beta) - m_\pi^2 + \beta) \Pi = 0, \quad (3.40)$$

where we have introduced the function $\beta(z) = g_5^2 e^{2A_s} v^2$. Defining the function $2B_\pi = A_s - \Phi + \log \beta$, then, introducing the transformation $\Pi = e^{-B_\pi} \psi_{\pi_n}$ we arrive at the Schrödinger equation

$$-\partial_z^2 \psi_{\pi_n} + V_\pi \psi_{\pi_n} = m_\pi^2 \psi_{\pi_n}, \quad (3.41)$$

with the potential given by

$$V_\pi = (\partial_z B_\pi)^2 - \partial_z^2 B_\pi + \beta. \quad (3.42)$$

At this point it is interesting to display a plot of the potential (3.42). This is shown in the left panel of Fig. 8 where we observe potential wells emerging in the different cases we have considered. For instance, for $\lambda = 2$ the potential barrier is bigger than $\lambda = 0$ and $\lambda = -2$. These potential wells, however, are not deep enough to allow a light state in the spectrum. This is related to the fact that the soft wall backgrounds considered in this work do not provide spontaneous symmetry breaking in the chiral limit and therefore we would not expect pseudo-Goldstone modes. In the right panel of Fig. 8 we display the potential obtained in the holographic model investigated in [23] where the potential well allows a lightest state in the spectrum, as reported in Ref. [23]. In Fig. 9 we show the evolution of the pseudoscalar meson masses

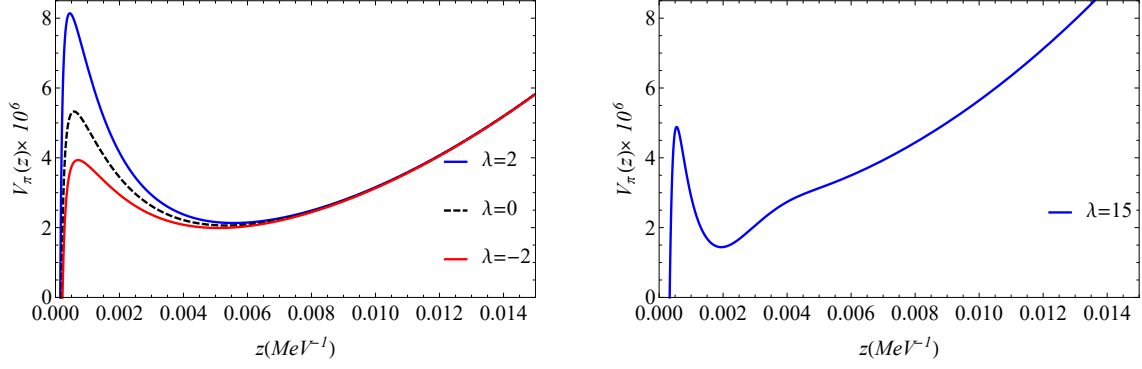


Figure 8. Left: The potential of the pseudoscalar Schrödinger equation in the NLSW model for $\lambda = 2$ (blue line), $\lambda = 0$ (dashed black line) and $\lambda = -2$ (red line), we have set $\phi_\infty = (388 \text{ MeV})^2$. Right: The potential of GKK model, this figure was obtained using the same parameters used in Ref. [23].

functions of the parameter C_0 (left panel) and c_1 (right panel), compared against the results of the linear soft wall model plotted with dashed lines. Note that the masses increase with the quark mass parameter c_1 , which is the expected behaviour of meson masses.

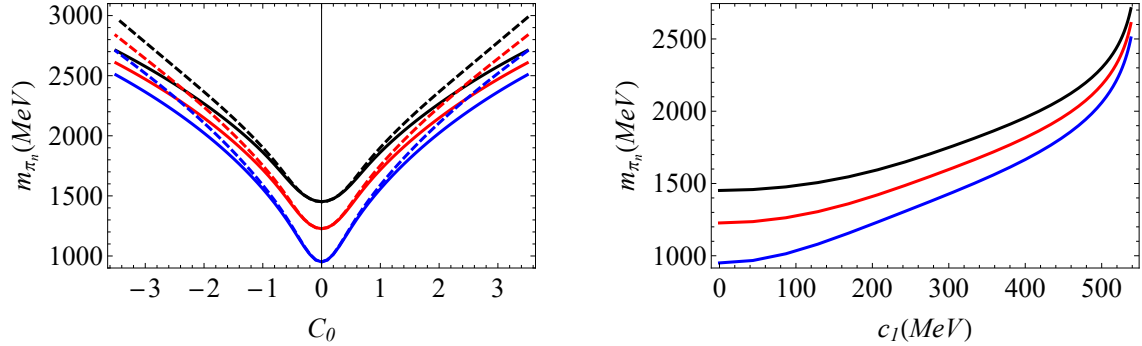


Figure 9. The mass as a function of C_0 (left) and c_1 (right). Solid lines represent the results for $\lambda = -2$, while dashed lines for $\lambda = 0$. The results were obtained setting $\phi_\infty = (388 \text{ MeV})^2$.

3.5 Meson spectrum ($\lambda > 0$)

As described in subsection 3.4.1, the spectrum of vector mesons is insensitive to the nonlinear potential so it is identical to the linear case ($\lambda = 0$). Below we describe the spectrum of scalar, axial-vector and pseudoscalar mesons for the case of positive λ , which corresponds to a Mexican hat potential in (3.1).

3.5.1 Spectrum of the scalar sector

The differential equation of the scalar sector, written in a Schrödinger form, was given in (3.34). The effect of going from negative to positive λ was displayed in

n	NLSW	SW [1]	GKK [11]	f_0 experimental [20]
1	980	950	799	980 ± 10
2	1246	1227	1184	1350 ± 150
3	1466	1452	1466	1505 ± 6
4	1657	1646	1699	1724 ± 7
5	1829	1820	1903	1992 ± 16
6	1986	1978	2087	2103 ± 8
7	2132	2125	2257	2314 ± 25
8	2268	2262	2414	

Table 2. The masses of the scalar mesons (in MeV) obtained in the nonlinear soft wall model with $\lambda > 0$, compared against the linear soft wall model [1], the holographic model of [11] and experimental data [20]. The value of the parameters are $\lambda = 7$, $C_0 = 0.3$ and $\phi_\infty = (388 \text{ MeV})^2$.

Fig. 5. We conclude that states become heavier for $\lambda > 0$ compared to the cases $\lambda = 0$ and $\lambda < 0$. We choose to fix the parameter C_0 , for given λ , by matching the mass of the first state to the $f_0(980)$ state. Our results for that parameter choice are displayed in Table 2, labeled as NLSW, compared against the linear soft wall, the holographic model [11] and experimental data. For $\lambda = 7$ we obtain $C_0 = 0.3$ and find $c_1 = 142.4(\text{MeV})$, which implies a large value for the quark mass. The main difference in relation to the case $\lambda < 0$ is that we cannot get the lightest state as $f_0(550)$. In Fig. 10 we show the evolution of the scalar meson masses as functions of the parameter C_0 (left panel) and c_1 (right panel). We observe that the masses increase with C_0 and c_1 . It is worth mentioning that in the chiral limit the mass of the scalar mesons are nonzero.

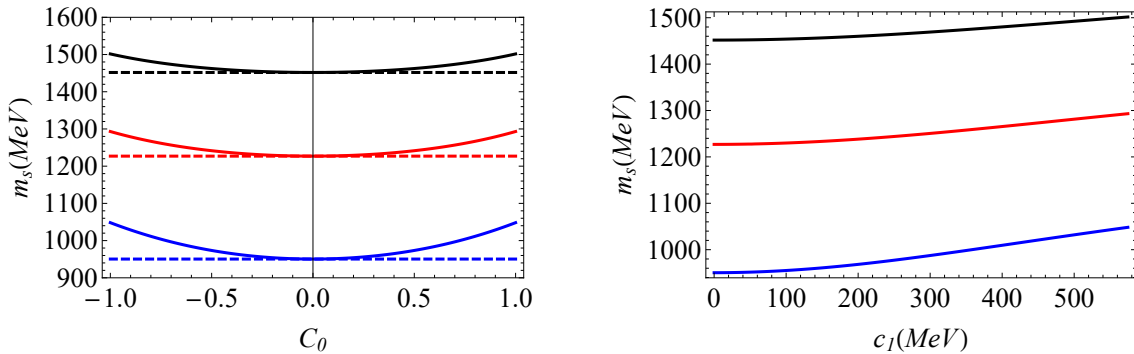


Figure 10. The masses of the scalar mesons as a function of C_0 (left panel) and c_1 (right panel). Solid lines represent the result for $\lambda = 2$, while dashed lines for $\lambda = 0$. The results were obtained setting $\phi_\infty = (388 \text{ MeV})^2$.

3.5.2 Spectrum of the axial-vector sector

The Schrödinger equation for the axial-vector sector was given in Eq. (3.36) and this time we consider the case $\lambda > 0$. Following the same procedure we have done for the $\lambda < 0$ case we find the axial-vector meson masses. In Fig. 11 we show the evolution of the masses as functions of the parameters C_0 (left panel) and c_1 (right panel), compared against the linear soft wall model ($\lambda = 0$) represented with dashed lines. The meson masses increase with the IR parameter C_0 and the UV quark mass parameter c_1 . Meson masses increasing with the quark mass is expected in QCD. It is also worth mentioning that in the chiral limit, i.e., $c_1 \rightarrow 0$, the masses of the axial-vector mesons are nonzero.

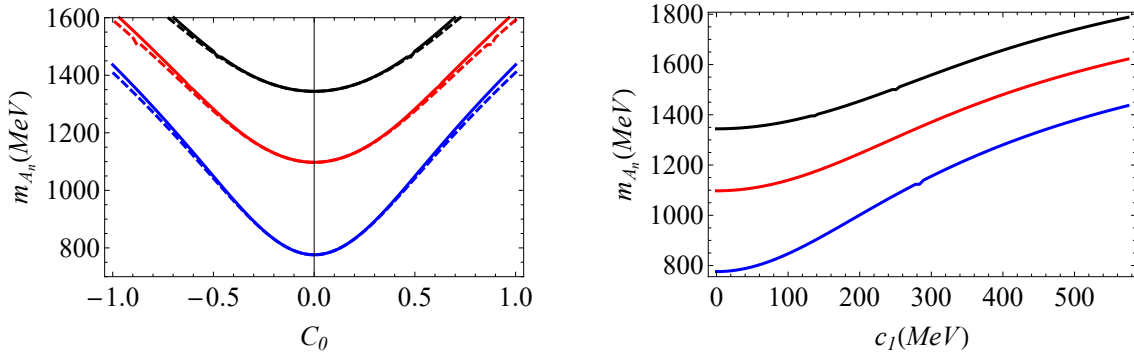


Figure 11. The masses of the axial-vector mesons as a function of C_0 (left panel) and c_1 (right panel). Solid lines represent the result for $\lambda = 2$, while dashed lines for $\lambda = 0$. The results were obtained setting $\phi_\infty = (388 \text{ MeV})^2$.

In Table 3 we present our results for the parameter choice $\lambda = 7$, $C_0 = 0.3$, fixed in the scalar sector. The results, labeled as NLSW, are compared against the linear soft wall model [1], the holographic model of [11] and experimental data [20]. We observe that our results are close to the results obtained in the linear soft wall model. This is explained by the smallness of the tachyon field for the parameters chosen to calculate the spectrum. For a small tachyon field the last term in the potential (3.37) is relatively small and the potential gets closer to the case of linear soft wall model. We also point out that in the nonlinear soft wall models presented in this work, the spectrum of the axial-vector and vector mesons are not degenerate, which is different from the linear soft wall model where they are degenerate.

3.5.3 Spectrum of the pseudoscalar sector

The pseudoscalar sector is described by the coupled equations (3.38)-(3.39). The system was decoupled and written in a Schrödinger form in (3.41) and this time we consider $\lambda > 0$. Fig. 12 shows our numerical results for the pseudoscalar meson masses as functions of the parameters C_0 (left panel) and c_1 (right panel). Again,

n	NLSW	SW [1]	GKK [11]	a_1 experimental [20]
1	897	891	1185	1230 ± 40
2	1172	1168	1591	1647 ± 22
3	1398	1395	1900	1930^{+30}_{-70}
4	1594	1592	2101	2096 ± 122
5	1770	1768	2279	2270^{+55}_{-40}
6	1930	1928		
7	2079	2077		

Table 3. The masses of the axial-vector mesons (in MeV) obtained in the nonlinear soft wall model, compared against the linear soft wall model [1], the holographic model of [11] and experimental data [20]. The value of the parameters used are $\lambda = 7$, $C_0 = 0.3$ and $\phi_\infty = (388 \text{ MeV})^2$.

we observe that the masses increase with with the quark mass parameter c_1 . Note that in the chiral limit $c_1 \rightarrow 0$ the mass of the first pseudoscalar state has a finite value. This result can be interpreted as the absence of pseudo-Goldstone bosons in the spectrum and support the background analysis leading to a vanishing chiral condensate in the chiral limit. T

The potential well in the IR observed in the Schrödinger potential in Fig. 8, is not deep enough to support the presente of a lightest state. Therefore, the first state arising in the right panel of Fig. 12 behaves as a pion resonance instead of a true pseudo-Goldstone boson. We will show in section 3.6 that all the decay constants for the pseudoscalar meson go to zero in the chiral limit $c_1 \rightarrow 0$, characterizing the pseudoscalar mesons as resonances.

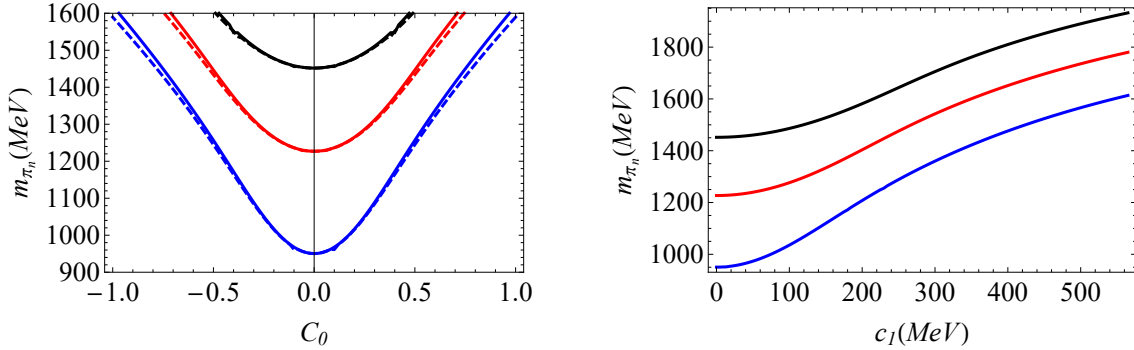


Figure 12. The masses of the pseudoscalar mesons as a function of C_0 (left panel) and c_1 (right panel). Solid lines represent the result for $\lambda = 2$, while dashed lines for $\lambda = 0$. The results were obtained setting $\phi_\infty = (388 \text{ MeV})^2$.

The spectrum obtained using the parameters $\lambda = 7$ and $C_0 = 0.3$, fixed in the scalar sector, is displayed in Table 4. Our results, labeled as NLSW, are compared

against the linear soft wall model [1], the holographic model of [23] and experimental data [20].

We also point out that the scalar and pseudoscalar sectors are not degenerate, in the nonlinear soft wall models, in contrast to the linear soft wall model.

n	NLSW	SW [1]	KBK [23]	π experimental [20]
1	-	-	144	140
2	1100	951	1557	1300 ± 100
3	1321	1227	1887	1816 ± 14
4	1518	1452	2090	2070
5	1697	1646	2270	2360
6	1861	1820	2434	
7	2013	1980	2586	

Table 4. The masses of the pseudoscalar mesons (in MeV) obtained in the nonlinear soft wall model with $\lambda > 0$, compared against the linear soft wall model [1], the holographic model of [23] and experimental data [20]. The value of the parameters are $\lambda = 7$ and $C_0 = 0.3$.

We finish this section showing in Fig. 13 the evolution of the parameters C_0 (left panel) and c_1 (right panel) when varying λ , matching the first scalar state to the meson $f_0(980)$. In this figure we observe why it is not possible to get small values for c_1 when λ is small. To get a small quark mass, for example, $m_q = 8\text{MeV}$, or equivalent to $c_1 = 2.21\text{MeV}$, the value of λ must be large, i.e., $\lambda = 3 \times 10^4$, with the corresponding value for $C_0 = 4.7 \times 10^{-3}$. Those results would have dramatic consequences in the spectrum, because the IR parameter C_0 would be so small that the contribution to the Schrödinger equations would be negligible and the spectrum of scalar and pseudoscalar mesons as well as vector and axial-vector mesons would be degenerate.

3.6 Decay constants

In this section, we calculate the decay constants of the vector, axial-vector and pseudoscalar mesons. In holographic QCD models the meson decay constants are related to the normalization constants for the field perturbations, see e.g. [24]. The normalization condition for the vector field is given by

$$\int dz e^{A_s - \Phi} v_m(z) v_n(z) = \delta_{mn}, \quad (3.43)$$

where $A_s = -\ln z$ is the AdS warp factor, $\Phi(z) = \phi_\infty z^2$ the dilaton and v_n is the vector meson mode related to the wave function by $v_n(z) = N_{v_n} e^{-Bv} \psi_{v_n}(z)$.

N_{v_n} is the normalization constant and ψ_{v_n} is solution of the Schrödinger equation (3.30). As described in appendix A, the decay constants are related to 4d conserved

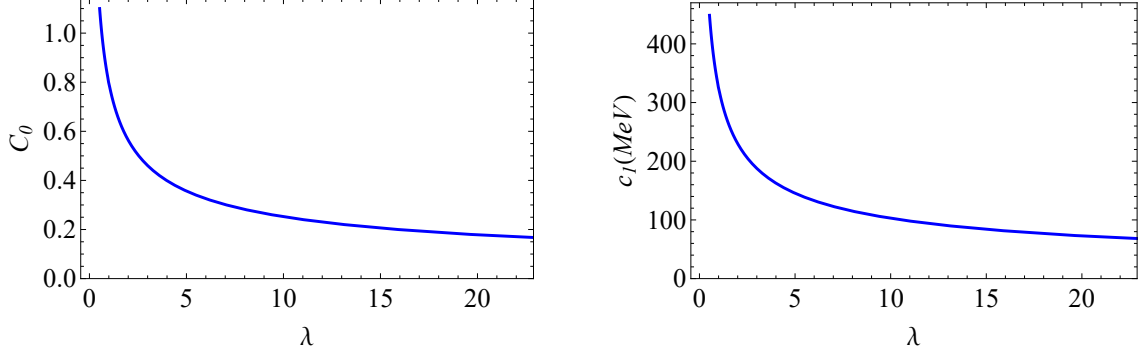


Figure 13. The evolution of C_0 as a function of λ (left panel) and c_1 as a function of λ (right panel), when matching the first scalar state to the meson $f_0(980)$. We remind the reader that $\phi_\infty = (388 \text{ MeV})^2$, fixed in the vector sector.

currents and they are defined through the relations in Eq. (A.21)

$$F_{v_n} = -\lim_{\epsilon \rightarrow 0} \frac{e^{A_s - \Phi}}{g_5} \partial_z v_n \Big|_{z=\epsilon} = \frac{2}{g_5} N_{v_n}. \quad (3.44)$$

Therefore, we observe that the decay constant depends on the normalization constant of the wave functions. We follow the same procedure for the axial-vector sector, where the normalization condition is given by

$$\int dz e^{A_s - \Phi} a_m(z) a_n(z) = \delta_{mn}, \quad (3.45)$$

where $a_m(z) = N_{a_n} e^{-B_A} \psi_{a_n}(z)$, N_{a_n} is the normalization constant and ψ_{a_n} is the solution of the Schrödinger equation (3.36). Thus, the decay constants are given by

$$F_{a_n} = -\lim_{\epsilon \rightarrow 0} \frac{e^{A_s - \Phi}}{g_5} \partial_z a_n \Big|_{z=\epsilon} = \frac{2}{g_5} N_{a_n}. \quad (3.46)$$

The problem of finding decay constants have reduced to the problem of calculating normalization constants of the wave functions. In the left panel of Fig. 14 we display the results for the decay constants of axial-vector mesons as functions of the quark mass parameter c_1 . The decay constants do not vary significantly in the region of small c_1 but they decrease at large c_1 approximately as $F_{a_1}^{1/2} \sim 1/c_1^b$, with $b = 2.6$. In Table 5 we display our numerical results for the ground state ($n = 1$) decay constants in the case $\lambda = 7$ and $C_0 = 0.3$.

For the pseudoscalar sector the normalisation condition is given by [24]

$$\int dz e^{A_s - \Phi} \beta(z) (\partial_z \pi_m) (\partial_z \pi_n) = m_{\pi_n}^2 \delta_{mn}. \quad (3.47)$$

There are different approaches to calculate the decay constants of pseudoscalar mesons in the literature. First of all, we consider the prescription used in hard wall

	NLSW ($\lambda > 0$)	SW [1]	experimental [20]
$F_\rho^{1/2}$	260.12	261	346.2 ± 1.4
$F_{a_1}^{1/2}$	215.37	261	433 ± 13

Table 5. The decay constants (in MeV) obtained in the nonlinear soft wall model, compared against the result obtained in the linear soft wall model Ref. [1] and experimental results of PDG [20]. The results for $\lambda > 0$ were obtained setting $\lambda = 7$ and $C_0 = 0.3$.

model [5] (see also [25, 26]). The authors considered the massless case, $m_\pi^2 = 0$. In that limit the pion decay constant can be extracted from the axial current correlator by the relation

$$f_\pi^2 = -\lim_{\epsilon \rightarrow 0} \frac{e^{A_s - \Phi}}{g_5^2} \partial_z A(0, \epsilon), \quad (3.48)$$

where $A(0, \epsilon)$ is the non-normalisable solution for the axial-vector field dual to the 4d axial-vector current. We point out that the prescription is valid only in the case $m_\pi^2 = 0$ and does not allow the investigation of pion resonances.

A prescription for calculating the decay constant for the pseudoscalar sector and their resonances was developed in [22]. Details on the derivation are given in appendix A. The holographic dictionary for the decay constant maybe written in the form

$$f_{\pi_n} = -\lim_{\epsilon \rightarrow 0} \frac{e^{A_s - \Phi}}{g_5} \partial_z \varphi_n(z) \Big|_{z=\epsilon}, \quad (3.49)$$

where $\varphi_n(z)$ is the normalised wave function satisfying the normalisation condition

$$\int dz \frac{e^{A_s - \Phi}}{\beta(z)} (\partial_z \varphi_m) (\partial_z \varphi_n) = \delta_{mn}. \quad (3.50)$$

In terms of $\partial_z \pi_n$ the decay constant is obtained by plugging Eq. (3.39) into Eq. (3.49)

$$f_{\pi_n} = -\lim_{\epsilon \rightarrow 0} \frac{e^{A_s - \Phi}}{g_5 m_{\pi_n}^2} \beta(z) \partial_z \pi_n(z) \Big|_{z=\epsilon}. \quad (3.51)$$

Hence, the normalization condition takes the form

$$\int dz e^{A_s - \Phi} \beta(z) (\partial_z \pi_m) (\partial_z \pi_n) = m_{\pi_n}^2 \delta_{mn}. \quad (3.52)$$

Finally, in terms of the Schrödinger wave function defined in Eq. (3.41), the decay constant takes the form

$$f_{\pi_n} = -\lim_{\epsilon \rightarrow 0} \frac{e^{(A_s - \Phi)/2}}{g_5 m_{\pi_n}^2} \beta^{1/2}(z) \psi_{\pi_n}(z) \Big|_{z=\epsilon}, \quad (3.53)$$

where the normalisation condition is given by

$$\int dz \psi_{\pi_m}(z) \psi_{\pi_n}(z) = m_{\pi_n}^2 \delta_{mn}. \quad (3.54)$$

At the end of the day, the decay constant depends only on the normalisation constant. Thus, the procedure above allows us to calculate the decay constant of the fundamental state and its resonances. In our calculations of the decay constant of the pseudoscalar mesons we have used the three formulae described above to show the consistency of our numerical results. In the right panel of Fig. 14 we plot the decay constants as a function of the parameter c_1 of the first three pseudoscalar mesons. For small values of c_1 the decay constant goes like $f_{\pi_1} = 0.46 c_1$, which is equivalent to the observed in the hard wall model in Ref. [24], the decay constants decrease for the resonances and scales with c_1 , i.e., the quark mass. This result is in agreement with the results predicted in QCD [27] (see also Ref. [28]). On the other hand, the behavior changes in the region where c_1 is heavier, where the decays constant decrease. It is worth mentioning that in Ref. [29] the authors indicated that the decay constant behaves as $f \sim 1/\sqrt{M}$, where M is the mass of the heavy-light mesons. In turn, the behavior of the numerical data displayed in the left panel of Fig. 14 goes approximately as $f_{\pi_1} \sim 1/c_1^a$, with $a = 4.4$.

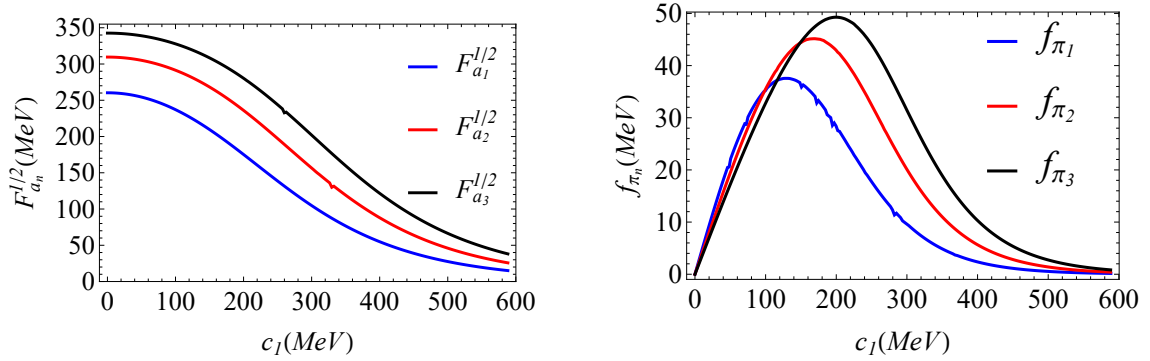


Figure 14. The decay constants of the axial-vector mesons (left panel) and pseudoscalar mesons (right panel) as a function of c_1 obtained in the NLSW model for $\phi_\infty = (388 \text{ MeV})^2$ and $\lambda = 2$.

Finally, numerical results are displayed in Table 6, we can see that the values of the decay constants increase for $C_0 = 0.4$ corresponding to $c_1 = 203.68 \text{ MeV}$, which lies in the region where the decay constants decrease, see for instance right panel of Fig. 14 (the results for $\lambda = 7$ are qualitatively the same). In turn, the decay constants for $C_0 = 0.1$ corresponding to $c_1 = 44.17 \text{ MeV}$ lies in the region where the decay constants increase with c_1 , in this region holds $f_{\pi_1} > f_{\pi_2} > f_{\pi_3}$, these results are consistent with the resonances.

4 Nonlinear soft wall models with running mass

Recent works in holographic soft wall model have considered the possibility of a tachyon squared mass m_X^2 depending on the radial coordinate z [30, 31]. The mo-

	f_{π_1}	f_{π_2}	f_{π_3}
NLSW ($C_0 = 0.4$)	27.20	40.84	47.36
NLSW ($C_0 = 0.1$)	19.63	17.25	15.25

Table 6. The decay constants (in MeV) obtained in the nonlinear soft wall model. The results for $\lambda = 7$ were obtained setting $C_0 = 0.4$ ($c_1 = 203.68\text{MeV}$), $C_0 = 0.1$ ($c_1 = 44.17\text{MeV}$) and $\phi_\infty = (388\text{MeV})^2$.

tivation for a tachyon running mass is to obtain a nontrivial IR contribution to the tachyon differential equation and therefore find a richer dynamics. In holography a 5d running mass for the tachyon would correspond to the anomalous dimension for the 4d quark mass operator [30, 32].

For the tachyon running mass we take the ansatz

$$m_X^2(z) = -3 - \phi_c z^2. \quad (4.1)$$

The tachyon differential equation now becomes

$$\left[z^2 \partial_z^2 - (3 + 2\phi_\infty z^2) z \partial_z + 3 + \phi_c z^2 \right] v - \frac{\lambda}{2} v^3 = 0. \quad (4.2)$$

4.1 Asymptotic analysis

In the UV we consider again the Frobenius ansatz

$$v(z) = c_1 z + d_3 z^3 \ln z + c_3 z^3 + d_5 z^5 \ln z + c_5 z^2 + \dots \quad (4.3)$$

Plugging this ansatz into (4.2) we find the UV coefficients

$$\begin{aligned} d_3 &= \frac{1}{4} c_1 (c_1^2 \lambda + 4\phi_\infty - 2\phi_c), \quad d_5 = \frac{1}{64} c_1 (-c_1^2 \lambda - 4\phi_\infty + 2\phi_c) (-c_1^2 \lambda - 12\phi_\infty + 2\phi_c), \\ c_5 &= \frac{1}{256} \left[-9c_1^5 \lambda^2 - (-24c_1^3 \phi_c + 56c_1^3 \phi_\infty + 48c_1^2 c_3) \lambda \right. \\ &\quad \left. - 12c_1 \phi_c^2 + 64c_1 \phi_c \phi_\infty - 80c_1 \phi_\infty^2 - 32c_3 \phi_c - 192c_3 \phi_\infty \right], \dots \end{aligned} \quad (4.4)$$

In the special case $c_1^2 \lambda + 4\phi_\infty - 2\phi_c = 0$ we have $d_3 = d_5 = 0$ and $c_5 = \frac{1}{4} \phi_c c_3$ so we do not expect logarithmic terms but there maybe another solution besides the linear solution $v(z) = c_1 z$ due to a nonzero c_3 .

In the IR we work with the variable $y = 1/z$. Eq. (4.2) becomes

$$\left[(y \partial_y)^2 + 2(2 + \phi_\infty y^{-2})(y \partial_y) + (3 + \phi_c y^{-2}) \right] v - \frac{\lambda}{2} v^3 = 0. \quad (4.5)$$

We take again the power ansatz

$$v^{IR}(y) = C_0 y^\alpha. \quad (4.6)$$

Plugging this ansatz into (4.5) we obtain the polynomial equation

$$C_0 y^\alpha (\alpha^2 + 4\alpha + 3) + C_0 y^{\alpha-2} (2\alpha\phi_\infty + \phi_c) - \frac{\lambda}{2} C_0^3 y^{3\alpha} = 0. \quad (4.7)$$

Again we distinguish 3 cases: $\alpha > -1$, $\alpha = -1$ and $\alpha < -1$. The latter case is trivial because it leads to $C_0 = 0$.

In the case $\alpha > -1$ the second term dominates and we find

$$\alpha = -\frac{\phi_c}{2\phi_\infty} \quad , \quad \phi_c < 2\phi_\infty. \quad (4.8)$$

This is a natural deformation of the regular solution found in the previous section. For $0 > \alpha > -1$ the solution is actually divergent and admits the expansion

$$v^{IR}(y) = y^\alpha (C_0 + C_2 y^\beta + \dots) \quad , \quad \beta = 2 - \frac{\phi_c}{\phi_\infty}, \quad (4.9)$$

with

$$C_2 = -\frac{C_0^3 \lambda}{4(\phi_c - 2\phi_\infty)}. \quad (4.10)$$

We will focus on the case $\phi_c = \phi_\infty$ where, in terms of z , the tachyon solution reads

$$v = C_0 \sqrt{z} \left(1 + \frac{C_0^2 \lambda}{4\phi_\infty} z^{-1} + \frac{3C_0^4 \lambda^2 - 10\phi_\infty}{32\phi_\infty^2} z^{-2} + \dots \right). \quad (4.11)$$

This is a divergent solution depending on only one parameter, C_0 . The IR leading behaviour $v \propto \sqrt{z}$ was considered as an IR constraint in a previous approach [33]

In the special case $\alpha = -1$, the first term in (4.7) vanishes whereas the second and third terms lead to the condition $-C_0^2 \lambda + 2\phi_c - 4\phi_\infty = 0$. This linear solution, i.e. $v(z) = C_0 z$ is valid only for $\lambda < 0$ and $\phi_c < 2\phi_\infty$.

Running mass with $\lambda = 0$

We finish this subsection pointing out that the divergent solution (4.9) survives in the case $\lambda = 0$. This corresponds to the linear soft wall model with running mass. In the case $\phi_c = \phi_\infty$, this solution has the following UV and IR behaviour

$$v^{UV}(z) = c_1 z + c_3 z^3 + \frac{c_1 \phi_\infty}{2} z^3 \ln z + \dots, \quad (4.12)$$

$$v^{IR}(z) = C_0 \sqrt{z} \left(1 - \frac{5}{16\phi_\infty} z^{-2} + \dots \right). \quad (4.13)$$

4.2 Numerical solution

The numerical results for the nonlinear soft wall model in the presence of a tachyon running mass are qualitatively similar to the case without the running mass. The main effect of the running mass will be extending the range for the IR parameter

C_0 . In particular, for the case $\lambda > 0$ the upper bound $C_0^2 \lambda < 6$ found in the previous section is not present anymore.

We present numerical results for the case $\phi_c = \phi_\infty$ corresponding to the IR behaviour (4.11). Fig. 15 displays the UV parameters c_1 and c_3 as functions of the IR parameter C_0 for different values of λ . Fig. 15 displays c_3 as a function of c_1 which can be interpreted in terms of the 4d chiral condensate as a function of the quark mass, as described in subsection 3.3. For the case $\lambda < 0$ we note a decrease

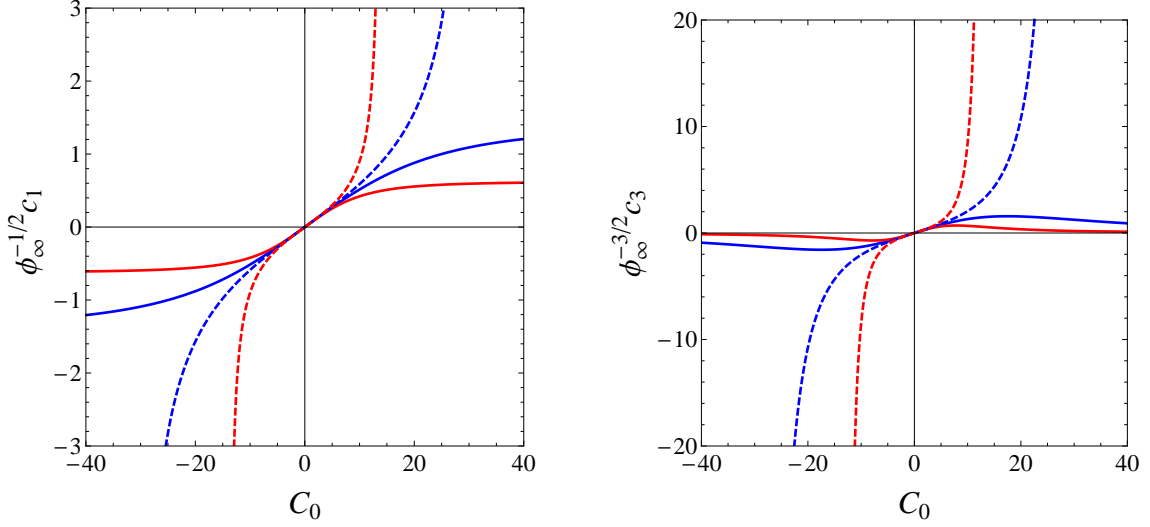


Figure 15. Numerical results for c_1 (left panel) and c_3 (right panel) as functions of C_0 in units of $\sqrt{\phi_\infty}$. The blue and red solid lines (dashed lines) correspond to $\lambda = -1$ and $\lambda = -5$ ($\lambda = 1$ and $\lambda = 5$).

in the range of c_1 and a lower maximum value for c_3 , when compared to the case without running mass described in the previous section. For the case $\lambda > 0$, despite having a bigger C_0 range, we do not notice a significant difference in c_3 vs c_1 when compared to the case without the running mass. Again, we conclude that the case $\lambda > 0$ provides the more realistic scenario for chiral symmetry breaking.

One of the motivations of considering a 5d running mass for the tachyon was to gain a nontrivial dynamics in the IR depending on the parameter ϕ_c in (4.1). However, we have found that the numerical results were very similar, despite having a background divergent in the IR. This may be related to the fact that the divergence is of the form $z^{-\alpha}$ with $0 < \alpha < 1$. As in the case without running mass, in the chiral limit $c_1 \rightarrow 0$ all the parameters go to zero. This is a negative result for the nonlinear soft wall models because it does not describe spontaneous symmetry breaking, expected in QCD in the chiral limit.

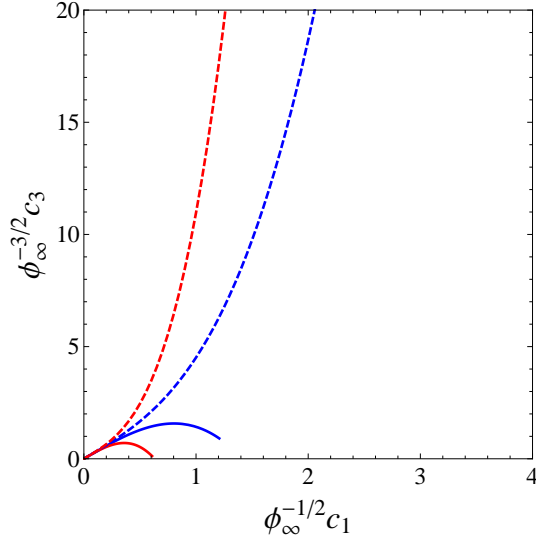


Figure 16. The VEV parameter c_3 as a function of the source parameter c_1 , in units of $\sqrt{\phi_\infty}$, for different values of λ . The blue and red solid lines (dashed lines) correspond to $\lambda = -1$ and $\lambda = -5$ ($\lambda = 1$ and $\lambda = 5$).

4.3 Meson Spectrum ($\lambda < 0$)

4.3.1 Spectrum of the scalar sector

The equation of the scalar sector is the same as Eq. (3.33). However, we must add the running mass term $m_X^2(z) = -3 - \phi_c z^2$. Considering the special case $\phi_\infty = \phi_c$, the profile of the tachyon field diverges in the IR region as $v \sim z^{1/2}$, we also expect a different behavior of the potential in the Schrödinger equation, i.e., (3.34), consequently different spectrum. A plot of the potential is displayed in Fig. 17 for different values of λ , we observe the main difference between the models with λ negative, zero or positive. For λ negative it is possible to get a lightest state, just like in the model without running mass, cf. Section 3.4.2. However, we are following a more conservative approach and considering $f_0(980)$ as the first scalar meson.

As a complementary analysis, in Fig. 18 we show the mass of the scalar mesons as a function of the parameter C_0 (left panel). From this figure we observe that the mass decreases with C_0 (solid lines), this explains why we may fix the parameters with a lightest the state. Right panel of Fig. 18 shows the evolution of the mass as a function of the quark mass, i.e., $c_1 \propto m_q$. However, the fact that the mass decreases is not expected. Seems that the same pathology arising in the model without running mass is arising in the model with running mass.

4.3.2 Spectrum of the axial-vector sector

The Schrödinger equation describing the axial-vector sector is the same as Eq. (3.36). As in the scalar sector analysis, we must add the running mass term. However, we

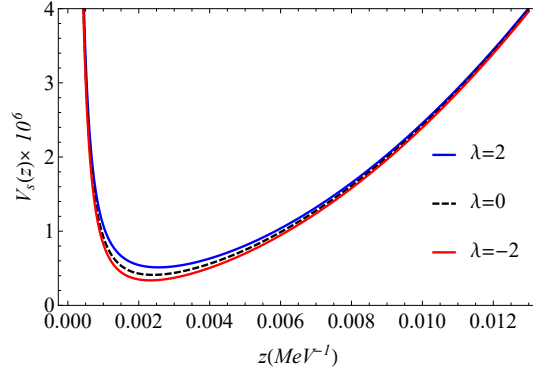


Figure 17. The potential of the Schrödinger equation of the scalar sector for $\phi_c = \phi_\infty = (388 \text{ MeV})^2$ and three different values of the parameter λ .

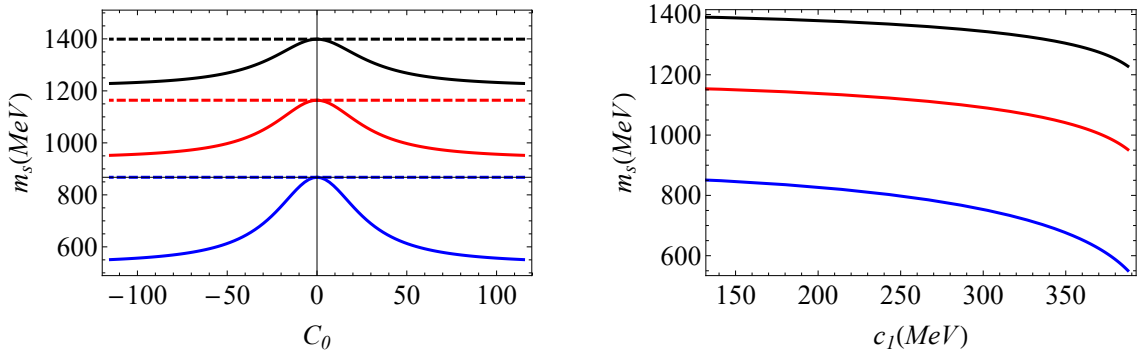


Figure 18. The mass of the scalar mesons as a function of C_0 (left panel) and c_1 (right panel). Solid lines represent the result for $\lambda = -2$, while dashed lines for $\lambda = 0$. The results were obtained setting $\phi_\infty = \phi_c = (388 \text{ MeV})^2$.

do not have interest in the spectrum because of the pathology observed in the scalar sector. In turn, we display results of the evolution of the mass (for the first three states) as a function of the parameter C_0 in the left panel of Fig. 19 with solid lines, while dashed lines represent the results for $\lambda = 0$. From this figure we can see that the mass increases as the parameter C_0 increases. On the other hand, we display results of the mass as a functions of the quark mass, i.e., c_1 , in the right panel of this figure. Initially, we observe that the mass of the axial-vector mesons increase slowly with the quark mass. Then, it increases rapidly, seems that there is a saturation value of the quark mass where the mass of the axial-vector mesons “blow up”.

4.3.3 Spectrum of the pseudoscalar sector

The coupled equations of the pseudoscalar mesons are the same as Eqs. (3.38) and (3.39). By combining these equations we reduced them into a Schrödinger form in Eq. (3.41). Using the same numerical procedure applied in the case without running

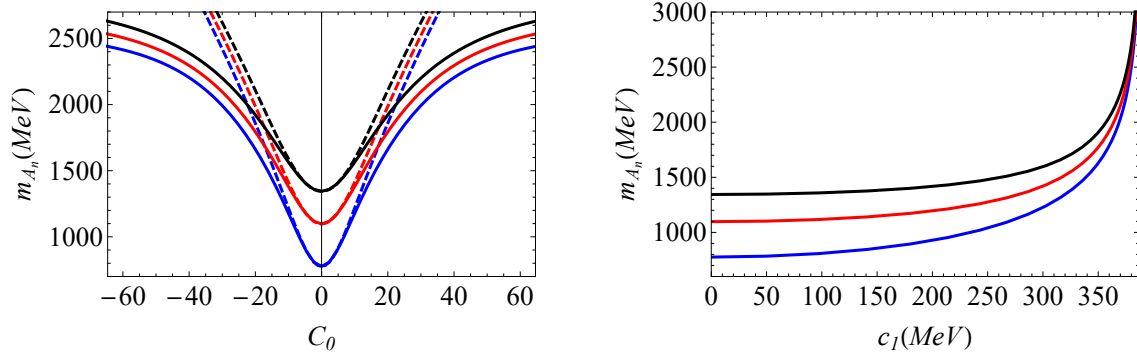


Figure 19. The mass of the axial-vector mesons as a function of C_0 (left panel) and c_1 (right panel). Solid lines represent the results for $\lambda = -2$, while dashed lines for $\lambda = 0$. The results were obtained setting $\phi_\infty = \phi_c = (388 \text{ MeV})^2$.

mass, we were able to get the mass as function of the parameters C_0 and c_1 , we display the numerical results in Fig. 20. In the left panel of this figure we show the variation of the mass as a function of C_0 with solid lines, while the results for $\lambda = 0$ are represented with dashed lines, we can see that the mass of the pseudoscalar mesons always increases with C_0 . We also point out that the mass increases faster close to $C_0 = 0$ and slowly for large values of C_0 . Meanwhile, in the right panel of this figure we display the evolution of the mass as a function of the quark mass, we also observe that the mass of the pseudoscalar mesons increase with c_1 , slowly in the region of small quark mass and faster in the intermediate and large quark mass region.

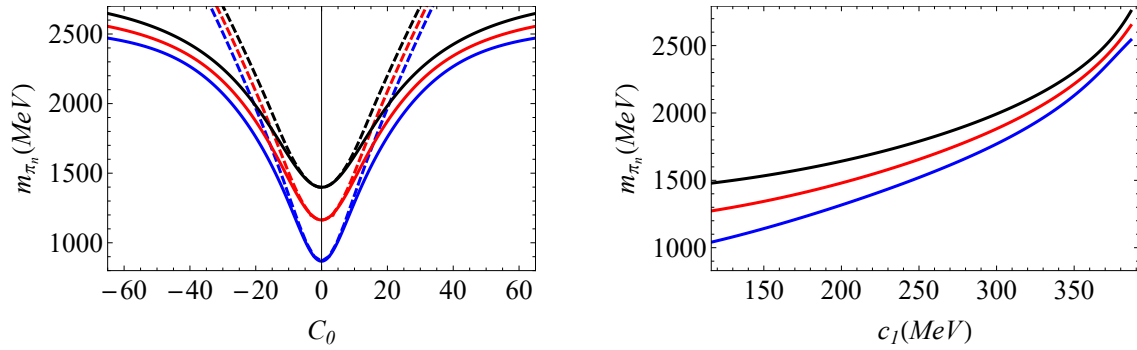


Figure 20. The mass of the pseudoscalar mesons as a function of C_0 (left panel) and c_1 (right panel). Solid lines represent the result for $\lambda = -2$, while dashed lines for $\lambda = 0$. The results were obtained setting $\phi_\infty = \phi_c = (388 \text{ MeV})^2$.

4.4 Meson Spectrum ($\lambda > 0$)

4.4.1 Spectrum of the scalar sector

The equation of the scalar sector is the same as Eq. (3.33). However, we must add the running mass term $m_X^2(z) = -3 - \phi_c z^2$. This way, we are adding a new parameter in the model, the additional term will guarantee a divergent solution in the IR region. In turn, the potential of the Schrödinger equation (3.34) is shown in Fig. 17 for $\lambda = 2$. Our numerical results of the mass as a function of C_0 are displayed in the left panel of Fig. 21, while for the mass as function of c_1 in the right panel of the same figure. From these results we can see that the mass is increasing with both parameters. Therefore, this allows us to use the same strategy implemented in Sec. 3.5.1 to fix the parameters, i.e., using the state $f_0(980)$. Having fixed the parameters and using a shooting method we calculate the spectrum, which are displayed in Table 7 as NLSW-RM. The fact that we calculate a spectrum compatible with results available in the literature does not guarantee that the value of the quark mass will be of the same order of a physical quark mass, i.e., $m_q = 8\text{MeV}$, for example. Hence, the parameters we obtain are $\lambda = 7$ and $C_0 = 7.6$, thus, the quarks mass becomes $m_q = 870\text{MeV}$, which is larger than quark mass obtained in the model without running mass, where we get $m_q = 516.6\text{MeV}$.

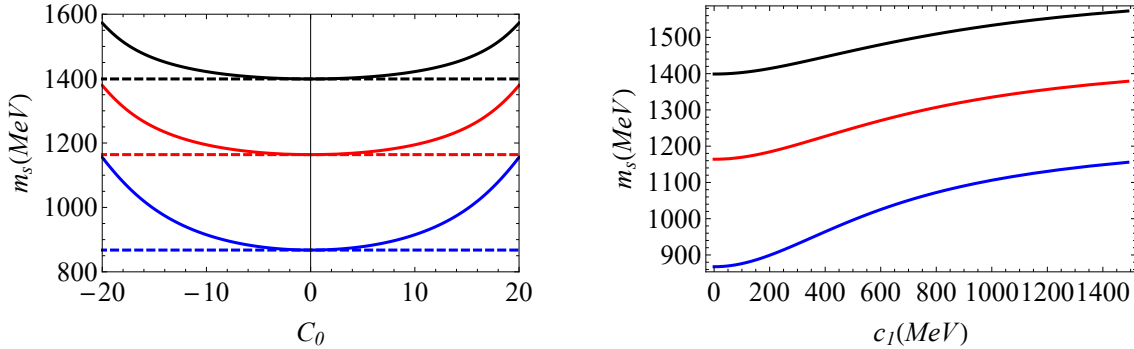


Figure 21. The mass of the scalar mesons as a function of C_0 (left panel) and c_1 (right panel). Solid lines represent the result for $\lambda = 2$, while dashed lines for $\lambda = 0$. The results were obtained setting $\phi_\infty = \phi_c = (388\text{MeV})^2$.

4.4.2 Spectrum of the axial-vector sector

The axial-vector sector is described by the same equations of Section 3.4.3, this time we must add the running mass term and change $\lambda \rightarrow -\lambda$. In a general case, the evolution of the mass as a function of the parameter C_0 is displayed in the left panel of Fig. 22 with solid lines, in this figure we can also see the results for $\lambda = 0$ with dashed lines. The right panel of Fig. 22 shows the mass as a function of the quark mass, i.e., $c_1 \propto m_q$. We can see that the mass of the axial-vector mesons increase

n	NLSW-RM	FLZ A [30]	GKK [11]	f_0 experimental [20]
1	980	586	799	980 ± 10
2	1238	1346	1184	1350 ± 150
3	1455		1466	1505 ± 6
4	1645	1743	1699	1724 ± 7
5	1816	2232	1903	1992 ± 16
6	1973	2420	2087	2103 ± 8
7	2118		2257	2314 ± 25
8	2255		2414	

Table 7. The masses of the scalar mesons (in MeV) obtained in the nonlinear soft wall model with running mass, compared against the results of Refs. [11, 30] and experimental results of PDG [20]. The value of the parameters used are $\lambda = 7$ and $C_0 = 7.6$.

slowly when c_1 is small, then, it increases faster in the intermediate region of c_1 , finally, the mass increases slowly again for large values of c_1 .

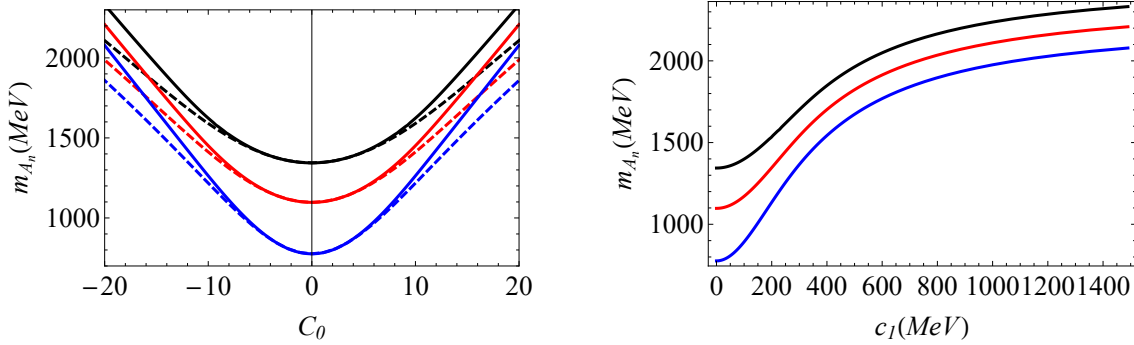


Figure 22. The mass of the axial-vector mesons as a function of C_0 (left panel) and c_1 (right panel). Solid lines represent the results for $\lambda = 2$, while dashed lines for $\lambda = 0$. The results were obtained setting $\phi_\infty = \phi_c = (388 \text{ MeV})^2$.

Having investigated the general case, i.e., considering parameters without any constraint, now we calculate the spectrum using the parameters we have used in the scalar sector, i.e., $\lambda = 7$ and $C_0 = 7.6$. The results are displayed in Table 8 as NLSW-RM. As before, we are considering the case when $\phi_\infty = \phi_c$.

It is worth mentioning that the spectrum is different from the spectrum of the vector mesons, cf. Table 1, which means that both sectors are not degenerate. This is explained because the tachyon field is divergent and the value of C_0 is not so small. This is also a signal that chiral symmetry was not restored.

n	NLSW-RM	FLZ A [30]	GKK [11]	a_1 experimental [20]
1	1147	1121	1185	1230 ± 40
2	1359	1608	1591	1647 ± 22
3	1547	1922	1900	1930^{+30}_{-70}
4	1718	2156	2101	2096 ± 122
5	1876	2352	2279	2270^{+55}_{-40}
6	2023	2526		
7	2161			

Table 8. The masses of the axial-vector mesons (in MeV) obtained in the nonlinear soft wall model with running mass, compared against the results of Refs. [11, 30] and experimental results of RPP [20]. The value of the parameters used are $\lambda = 7$, $C_0 = 7.6$ and $\phi_\infty = \phi_c = (388 \text{ MeV})^2$.

4.4.3 Spectrum of the pseudoscalar sector

The pseudoscalar mesons are described by the same equations of Section 3.4.4, including the running mass term and changing $\lambda \rightarrow -\lambda$. In the general case, the evolution of the mass as a function of the parameter C_0 is displayed in the left panel of Fig. 23 with solid lines, while dashed lines represent the results for $\lambda = 0$. In turn, the mass as a function of the quark mass is displayed in the right panel of Fig. 23. In both cases we can see that the mass increases. As a function of the quark mass, the mass increases slowly for small values of c_1 , then, it increases faster in the intermediate region of c_1 , finally, it increases slowly for large values of c_1 . From this figure we also see that there is not a Nambu-Goldstone-like particle, and the spectrum we calculate takes into account just the resonances.

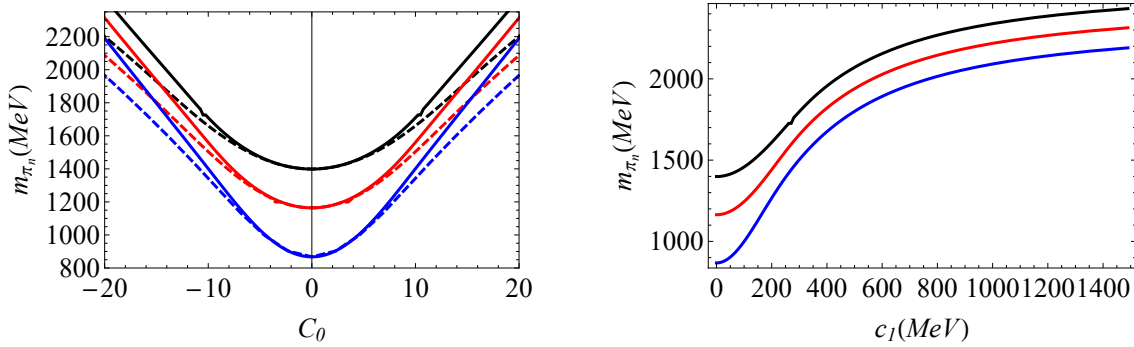


Figure 23. The mass of the pseudoscalar mesons as a function of C_0 (left panel) and c_1 (right panel). Solid lines represent the result for $\lambda = 2$, while dashed lines for $\lambda = 0$. The results were obtained setting $\phi_\infty = \phi_c = (388 \text{ MeV})^2$.

To calculate the spectrum we use the same parameters fixed in the scalar sector, i.e., $\lambda = 7$ and $C_0 = 7.6$. Our numerical results of the spectrum are displayed in

Table 9 as NLSW-RM. As can be seen, the mass of the Nambu-Goldstone-like state is missing, and the model allows us to calculate the spectrum of the resonances. We also compared our results against the results available in Refs. [23, 30] and the experimental one.

n	NLSW-RM	FLZ A [30]	KBK [23]	π experimental [20]
1	-	139.6	144	140
2	1301	1269	1557	1300 ± 100
3	1479	1753	1887	1816 ± 14
4	1642	2051	2090	2070
5	1796	2277	2270	2360
6	1942	2467	2434	
7	2081		2586	

Table 9. The masses of the pseudoscalar mesons (in MeV) obtained in the nonlinear soft wall model with running mass, compared against the results of Refs. [23, 30] and experimental results of RPP [20]. The value of the parameters used are $\lambda = 7$, $C_0 = 7.6$ and $\phi_\infty = \phi_c = (388 \text{ MeV})^2$.

Finally, we justify why it is not possible to get a physical quarks mass, i.e., $c_1 = 2.21 \text{ MeV}$, which is equivalent to $m_q = 8 \text{ MeV}$ for values of the parameter λ close to the linear soft wall model, i.e., $\lambda = 0$. In the left panel of Fig. 24 we show the results of C_0 as a function of λ , while in the right panel we show results of c_1 as a function of λ . These results were obtained by imposing that the first solution of the scalar sector is $m_s = 980 \text{ MeV}$. From the last figure we can see that c_1 is small just when λ is large and negative, for that reason, if we impose an additional condition that $c_1 = 2.21 \text{ MeV}$ we get $\lambda = 6.1 \times 10^3$ and $C_0 = 0.25$. Thus, considering these values to calculate the spectrum we conclude that the vector and axial-vector sectors are degenerate, the same is true for the scalar and pseudoscalar sectors, this is explained because the value of the tachyon field in the IR region is small.

4.5 Decay constants

In this section, we calculate the decay constants of the vector, axial and pseudoscalar mesons in the nonlinear soft wall model with running mass. As explained in Section 3.6, the decay constants are related to normalization condition on the fields. In the general case, we can calculate the evolution of the decay constants of the axial-vector and pseudoscalar mesons as a function of the quark mass, i.e., c_1 . In the left panel of Fig. 25 we display the evolution of the decay constants of the first three axial-vector mesons, the results are qualitatively the same as the results in the nonlinear soft wall model without running mass, cf. left panel of Fig. 14. In

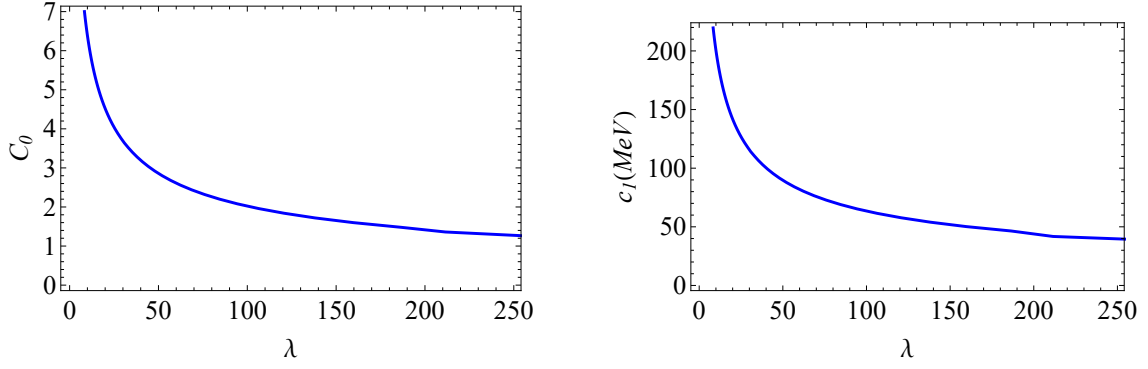


Figure 24. The evolution of C_0 as function of λ (left panel) and c_1 as a function of λ (right panel). The results were obtained setting $\phi_\infty = (388 \text{ MeV})^2$.

turn, the evolution of the decay constants of the first three pseudoscalar mesons are displayed in the right panel of Fig. 25, again, the results are qualitatively the same as the results displayed in the right panel of Fig. 14.

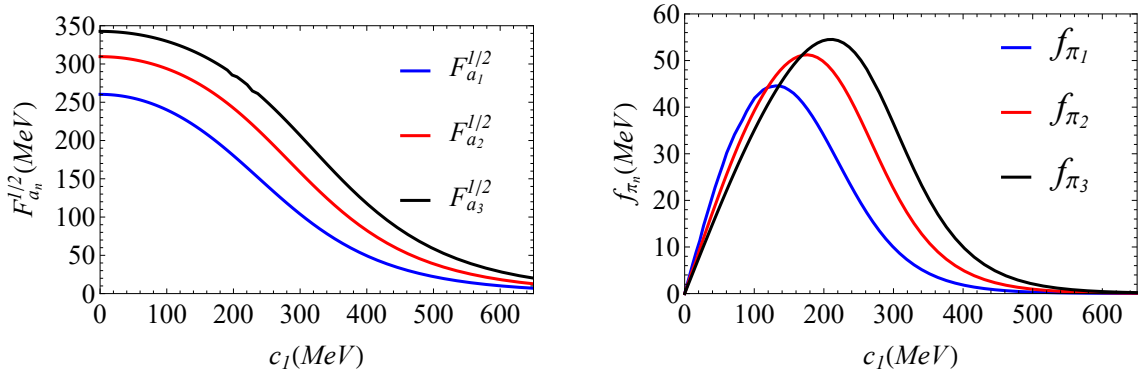


Figure 25. The decay constants of the axial-vector mesons (left panel) and pseudoscalar mesons (right panel) as a function of c_1 obtained in the NLSW model with running mass for $\phi_\infty = \phi_c = (388 \text{ MeV})^2$ and $\lambda = 2$.

Considering the specific case where we have fixed the parameters in the scalar sector, we may calculate the decay constants of the first state of the vector and axial-vector mesons. These results are displayed in Table 10 as NLSW-RM.

In turn, In Table 11 we calculate the decay constants for the first three pseudoscalar mesons. However, the values increase instead of decrease, this behavior may be explained because of the value $C_0 = 7.6$ corresponding to $c_1 = 237.20 \text{ MeV}$, value that lies in the heavy-light region, as can be seen in the right panel of Fig. 25 (the results for $\lambda = 2$ and $\lambda = 7$ are qualitatively the same). Nevertheless, if we consider $C_0 = 2$ we get $c_1 = 4.25 \text{ MeV}$, in this region the decay constants decrease, see right panel of Fig. 25, which means that the decay constants correspond to resonances.

	NLSW-RM ($\lambda > 0$)	FLZ A [30]	Exp. [20]
$F_\rho^{1/2}$	260.12	296	346.2 ± 1.4
$F_{a_1}^{1/2}$	152.78	389	433 ± 13

Table 10. The decay constants (in MeV) obtained in the nonlinear soft wall model with running mass, compared against the results of Refs. [11, 30] and experimental results of PDG [20]. The results were obtained setting $\lambda = 7$, $C_0 = 7.6$ and $\phi_\infty = \phi_c = (388\text{MeV})^2$.

This is supported by the results displayed in the right panel of Fig. 25, which are in agreement with results expected in QCD [27].

	f_{π_1}	f_{π_2}	f_{π_3}
NLSW-RM ($C_0 = 7.6$)	21.81	37.58	48.11
NLSW-RM ($C_0 = 0.2$)	2.45	1.93	1.63

Table 11. The decay constants of the first three pseudoscalar mesons (in MeV) obtained in the nonlinear soft wall model with running mass. The results were obtained setting $\lambda = 7$, $C_0 = 7.6$ ($c_1 = 237.2\text{MeV}$), $C_0 = 0.2$ ($c_1 = 4.25\text{MeV}$) and $\phi_\infty = \phi_c = (388\text{MeV})^2$.

5 Discussion and conclusions

In this work we have investigated a nonlinear realisation for chiral symmetry breaking in soft wall models based on a Higgs potential. Soft wall models allow for a more realistic description of the meson spectrum because a positive quadratic dilaton in the IR guarantees linear Regge trajectories. Solving the nonlinear differential equation of the tachyon we found that the tachyon solution in the IR depends on only one parameter C_0 . Integrating numerically the tachyon differential equation we found non-trivial relations between the UV parameters c_1 and c_3 and the IR parameter C_0 . Moreover, implementing the procedure of holographic renormalisation we obtained a dictionary for the 4d chiral condensate in terms of the VEV parameter c_3 . This allows us to find the evolution of the 4d chiral condensate with the quark mass. For the case $\lambda > 0$, corresponding to a Mexican hat Higgs potential, we found that the chiral condensate grows nonlinearly with the quark mass, as expected in QCD. We found, however, that a nonlinear Higgs potential for the tachyon is not sufficient to provide spontaneous symmetry breaking in the chiral limit because the chiral condensate vanishes as the quark mass goes to zero.

We have calculated the spectrum of the scalar, vector, axial-vector and pseudoscalar mesons. The spectrum of vector mesons decouples from the other sectors and their solutions are the same as in the linear soft wall model. We concluded that the case $\lambda > 0$, corresponding to a Mexican hat Higgs potential, provides the

most realistic scenario for the meson spectrum and decay constants. The spectrum of the scalar mesons present some kind of pathology in the case $\lambda < 0$, because the masses decrease when the quark mass increases. In the case $\lambda > 0$ we found that it is possible to match the $f_0(980)$ state by fixing appropriately the parameters λ and C_0 . The analysis of the spectrum showed us that the vector and axial-vector mesons are not degenerate, cf. Tables 1 and 3. In turn, the scalar and pseudoscalar mesons are not degenerate, cf. Tables 2 and 4. However, following that procedure we found a very large value for the quark mass. In fact, it is not possible to obtain a small quark mass, for example, $m_q = 8\text{MeV}$, without increasing λ , cf. right panel of Fig. 13. We calculated the decay constants of the vector, axial-vector and pseudoscalar mesons. For the axial-vector mesons the decay constants do not vary significantly in the region of small quark mass, however, they decrease in the region of large quark mass, cf. left panel of Fig. 14. For the pseudoscalar mesons, all the decay constants go to zero in the chiral limit, cf. right panel of Fig. 14, showing us that they represent pion resonances, indicating the absence of pseudo-Goldstone bosons. Even though the potential of the Schrödinger equation presents a potential well, cf. left panel of Fig. 8, this is not deep enough to support the emergence of a light state. A commentary apart deserves the decreasing behavior of the pseudoscalar decay constants in the regime of large quark mass, cf. Fig. 14.

As an attempt to allow for spontaneous symmetry breaking in the chiral limit, we also investigated nonlinear soft wall models with a tachyonic running mass. The consequence of the running mass was to increase the interval of C_0 in relation to the model without running mass. However, we realised that the results are qualitatively similar to the case without running mass. Again, we found that $\lambda > 0$ provides the most realistic scenario for the meson spectrum and decay constants and we were able to match again the $f_0(980)$ state in the scalar sector by fixing appropriately the parameters. Again, we found that fixing the parameter to describe the meson spectrum leads to a very large value for the quark mass. The results shown that the vector and axial-vector mesons are not degenerate cf. Tables 1 and 8, the same is true for the scalar and pseudoscalar mesons, cf. Tables 7 and 9.

Let us discuss briefly some other approaches to the problem of chiral symmetry in holographic QCD. The model proposed for Iatrakis-Kiritsis-Paredes Ref. [10] (see also Ref. [34]), which implemented the ideas of Ref. [35]. The authors in [10] claim that the tachyon must blow up in the IR when the background has confinement properties. This statement is related to the Coleman-Witten-like theorem [2]. As in our case, the IR tachyon solution in [10] depends only on one parameter. In contrast to our case, the model in [10] leads to spontaneous chiral symmetry breaking in the chiral limit. Running mass models were considered in [31],[36] and [30] as an attempt to allow for spontaneous symmetry breaking in the chiral limit. We have found, however, that in a consistent description of nonlinear soft wall models based on a Higgs potential, the tachyon running mass does not solve the lack of spontaneous

symmetry breaking in the chiral limit.

An interesting approach to the problem of chiral symmetry breaking is considering a negative profile of the dilaton [9]. A negative dilaton profile has some issues, see for instance Ref. [37] for a discussion. For example, it would violate the null energy condition in the gravitational background [38]. Nevertheless, the authors of Ref. [9] proposed that the profile of the dilaton in the UV may be negative, while in the IR must be positive in order to guarantee confinement and Regge-like behavior. They claim that in this way is possible to describe spontaneous chiral symmetry breaking in the chiral limit.

In conclusion, nonlinear soft wall models based on a Higgs potential (with and without a tachyon running mass) and a positive quadratic dilaton do not provide spontaneous chiral symmetry breaking in the chiral limit, as in QCD. Consequently, there are no pseudo-Goldstone bosons in the spectrum of pseudoscalar mesons. This conclusion is supported by the study of masses and decay constants in the region of small quark mass. We found, however, in the case $\lambda > 0$ a very reasonable behaviour for the chiral condensate in the regime of large quark mass, similar to the behaviour expected in QCD. For the case $\lambda > 0$ we also found a reasonable behaviour for all the meson masses as growing functions of the quark mass. Interestingly, we found that the decay constants of axial-vector mesons and pseudoscalar mesons decrease in the regime of large quark mass. This behaviour is also expected in QCD and encourages us to continue the investigation of nonlinear soft wall models. Finally, a natural extension of this work would be the investigation of backreacted Einstein-Dilaton backgrounds, where the confinement criterion is satisfied. This would allow for a consistent description of confinement and chiral symmetry breaking in a minimal holographic setup.

Acknowledgments

The authors would like to thank Carlsson Millser for stimulating discussions during the early stages of this project. The authors would also like to acknowledge very useful conversations with Saulo Diles, Diego Rodrigues, Jonathan Shock and Dimitrios Zoakos during the development of this work. A.B-B would like to thank the organizers of WONPAQCD 2019 for providing a stimulating environment. The work of A.B-B is partially funded by Conselho Nacional de Desenvolvimento Científico e Tecnológico (CNPq), grants No. 306528/2018-5 and No. 434523/2018-6. L. A. H. M. has financial support from Coordenação de Aperfeiçoamento de Pessoal de Nível Superior - Programa Nacional de Pós-Doutorado (PNPD/CAPES, Brazil).

A Equations of motion and decay constants

In this Appendix we write details about the derivation of the equations of motion used to calculate the meson spectrum as well as the holographic dictionary for meson decay constants. We will expand the action (3.2) up to second order on the fields and take the 5d metric as in (2.1).

We follow Ref. [24] (see also [39]). For simplicity, we take $N_f = 2$ and assume isospin symmetry ($m_u = m_d$). First we decompose the bifundamental field X in the form

$$X = e^{2i\pi^a T^a} \left(\frac{1}{2}v(z) + S \right), \quad (\text{A.1})$$

where $\pi^a(x^\mu, z)$ is the pseudoscalar field, T^a are the generators of $SU(2)$ and $S(x^\mu, z)$ the scalar fluctuation related to the scalar mesons. We also rewrite the fluctuation for the gauge fields as

$$A_m^{(L/R)} = V_m \pm A_m, \quad (\text{A.2})$$

where $V^m = V_a^m T^a$ and $A^m = A_a^m T^a$ are the vector and axial fields, respectively. Plugging (A.1) and (A.2) into the action (3.2) and expanding on the fields π^a , V_a^m and A_a^m up to second order we obtain $S = S_0 + S_2 + \dots$ with S_0 the effective 1d action for the background $v(z)$ and

$$S_2 = - \int dx^5 \sqrt{-g} e^{-\Phi} \left[2(\partial_m S)^2 + 2m_X^2 S^2 + 3\lambda v^2(z) S^2 + \frac{1}{4g_5^2} v_a^{mn} v_{mn}^a + \frac{1}{4g_5^2} a_a^{mn} a_{mn}^a + \frac{1}{2} v^2(z) (\partial_m \pi_a - A_{m,a})^2 \right], \quad (\text{A.3})$$

the action describing the kinetic terms for the 5d field fluctuations π^a , V_a^m and A_a^m . We have defined the Abelian tensors

$$v_{mn}^a = \partial_m V_n^a - \partial_n V_m^a, \quad a_{mn}^a = \partial_m A_n^a - \partial_n A_m^a \quad (\text{A.4})$$

To obtain the Euler-Lagrange equations we write the action as $S_2 = \int dx^5 \mathcal{L}_2$. The variation takes the form

$$\begin{aligned} \delta S_2 = & \int d^5x \left[\left(\frac{\partial \mathcal{L}_2}{\partial S} - \partial_m P_S^m \right) \delta S + \left(\frac{\partial \mathcal{L}_2}{\partial V_l^a} - \partial_m P_{V,a}^{ml} \right) \delta V_l^a + \left(\frac{\partial \mathcal{L}_2}{\partial A_l^a} - \partial_m P_{A,a}^{ml} \right) \delta A_l^a \right. \\ & \left. + \left(\frac{\partial \mathcal{L}_2}{\partial \pi^a} - \partial_m P_{\pi,a}^m \right) \delta \pi^a \right] + \int dx^5 \partial_m (P_S^m \delta S + P_{V,a}^{ml} \delta V_l^a + P_{A,a}^{ml} \delta A_l^a + P_{\pi,a}^m \delta \pi^a), \end{aligned} \quad (\text{A.5})$$

where P_S^m , $P_{V,a}^{ml}$, $P_{A,a}^{ml}$ and $P_{\pi,a}^m$ are the conjugate momenta associated with the scalar, vector, axial-vector and pseudoscalar fields, respectively. Explicitly, the conjugate

momenta are given by

$$\begin{aligned}
P_S^m &= \frac{\partial \mathcal{L}_2}{\partial(\partial_m S)} = -4e^{-\phi} \sqrt{-g} \partial^m S, & P_{V,a}^{ml} &= \frac{\partial \mathcal{L}_2}{\partial(\partial_m V_l^a)} = -\frac{e^{-\phi}}{g_5^2} \sqrt{-g} v_a^{ml}, \\
P_{A,a}^{ml} &= \frac{\partial \mathcal{L}_2}{\partial(\partial_m A_l^a)} = -\frac{e^{-\phi}}{g_5^2} \sqrt{-g} a_a^{ml}, \\
P_{\pi,a}^m &= \frac{\partial \mathcal{L}_2}{\partial(\partial_m \pi^a)} = -e^{-\phi} \sqrt{-g} v^2(z) (\partial^m \pi^a - A^{m,a}).
\end{aligned} \tag{A.6}$$

In turn, the derivatives of the Lagrangian are:

$$\begin{aligned}
\frac{\partial \mathcal{L}_2}{\partial S} &= -e^{-\phi} \sqrt{-g} [4m_X^2 - 6v^2(z)] S, & \frac{\partial \mathcal{L}_2}{\partial V_l^a} &= -0, \\
\frac{\partial \mathcal{L}_2}{\partial A_l^a} &= e^{-\phi} \sqrt{-g} v^2(z) (\partial^l \pi^a - A^{l,a}), & \frac{\partial \mathcal{L}_2}{\partial \pi^a} &= 0.
\end{aligned} \tag{A.7}$$

From these results we find that the equation of motion of the vector sector takes the form

$$\frac{e^\phi}{\sqrt{-g}} \partial_m (e^{-\phi} \sqrt{-g} v_a^{ml}) = 0. \tag{A.8}$$

The Abelian field strength was defined in (A.4). Working in the axial gauge $V_z^a = 0$, we get

$$e^{-A_s + \Phi} \partial_z (e^{A_s - \Phi} \partial_z V_{\nu,a}) + \square V_{\nu,a} = 0. \tag{A.9}$$

The equation of motion of the scalar sector takes the form

$$\frac{e^\phi}{\sqrt{-g}} \partial_m (e^{-\phi} \sqrt{-g} g^{mn} \partial_n S) - \left(m_X^2 + \frac{3}{2} \lambda v^2 \right) S = 0, \tag{A.10}$$

which may be written in the form

$$e^{-3A_s + \Phi} \partial_z (e^{3A_s - \Phi} \partial_z S) + \square S - e^{2A_s} \left(m_X^2 + \frac{3}{2} \lambda v^2 \right) S = 0, \tag{A.11}$$

The remaining equations of motion are

$$\begin{aligned}
\frac{e^\phi}{\sqrt{-g}} \partial_m (e^{-\phi} \sqrt{-g} a_a^{ml}) + v^2(z) g_5^2 (\partial^l \pi^a - A^{l,a}) &= 0, \\
\partial_m \left[e^{-\phi} \sqrt{-g} v^2(z) g_5^2 (\partial^m \pi^a - A^{m,a}) \right] &= 0.
\end{aligned} \tag{A.12}$$

We work in the axial gauge, $A_z^a = 0$, and decompose the gauge field as $A_b^\mu = A_{b\perp}^\mu + \partial^\mu \varphi_b$, where $A_{b\perp}^\mu$ is the transverse part and $\partial^\mu \varphi_b$ the longitudinal part. The transverse part leads to the equation of motion for the axial-vector sector

$$e^{A_s - \Phi} \partial_z (e^{A_s - \Phi} \partial_z A_{\perp}^{\mu,a}) + \square A_{\perp}^{\mu,a} - v^2(z) g_5^2 e^{2A_s} A_{\perp}^{\mu,a} = 0, \tag{A.13}$$

For the pseudoscalar sector we find the coupled equations

$$e^{A_s - \Phi} \partial_z (e^{A_s - \Phi} \partial_z \varphi^a) + v^2(z) g_5^2 e^{2A_s} (\pi^a - \varphi^a) = 0, \quad (\text{A.14})$$

$$- \partial_z \square \varphi^a + v^2(z) g_5^2 e^{2A_s} \partial_z \pi^a = 0. \quad (\text{A.15})$$

The dictionary for the decay constants is obtained from the holographic currents. The latter arise in the surface term of (A.5), which may be written as

$$\delta S_2^{\text{Bdy}} = - \int dx^4 \left(\langle J_s \rangle (\delta S) + \langle J_{V,a}^\mu \rangle (\delta V_\mu^a) + \langle J_{A,a}^\mu \rangle (\delta A_\mu^a) + \langle J_{\pi,a} \rangle (\delta \pi^a) \right)_{z=\epsilon} \quad (\text{A.16})$$

The VEV of 4d operators appearing in (A.16) are defined by

$$\begin{aligned} \langle J_s \rangle &= P_s^z = -4e^{-\Phi} \sqrt{-g} \partial^z S, & \langle J_{V,a}^\mu \rangle &= P_{V,a}^{z\mu} = -\frac{e^{-\Phi}}{g_5^2} \sqrt{-g} v^{z\mu}, \\ \langle J_{A,a}^\mu \rangle &= P_{A,a}^{z\mu} = -\frac{e^{-\Phi}}{g_5^2} \sqrt{-g} a^{z\mu}, & \langle J_{\pi,a} \rangle &= P_{\pi,a}^z = -e^{-\Phi} \sqrt{-g} v^2(z) (\partial \pi^a - A^{z,a}). \end{aligned} \quad (\text{A.17})$$

We identify $\langle J_{V,a}^\mu \rangle$ and $\langle J_{A,a}^\mu \rangle$ as the holographic vector and axial currents leading to the meson decay constants. The next step is to decompose the fields into their Kaluza-Klein modes as follows.

$$\begin{aligned} S(x, z) &= \sum_{n=0}^{\infty} s_n(z) \hat{S}_n(x), & V_a^\mu(x, z) &= g_5 \sum_{n=0}^{\infty} v_{a,n}(z) \hat{V}_{a,n}^\mu(x), \\ A_a^{\mu,\perp}(x, z) &= g_5 \sum_{n=0}^{\infty} a_{a,n}(z) \hat{A}_{a,n}^\mu(x), & \pi_a(x, z) &= g_5 \sum_{n=0}^{\infty} \pi_{a,n}(z) \hat{\pi}_{a,n}(x), \\ \varphi_a(x, z) &= g_5 \sum_{n=0}^{\infty} \varphi_{a,n}(z) \hat{\pi}_{a,n}(x). \end{aligned} \quad (\text{A.18})$$

Plugging (A.18) into the vector and axial-vector currents (A.17) we obtain the expansions

$$\begin{aligned} \langle J_{V,a}^\mu \rangle &= \sum_n \left(-\frac{e^{A_s - \Phi}}{g_5} \partial_z v_{a,n}(z) \right) \hat{V}_{a,n}^\mu(x), \\ \langle J_{A,a}^\mu \rangle &= \sum_n \left(-\frac{e^{A_s - \Phi}}{g_5} \partial_z a_{a,n}(z) \right) \hat{A}_{a,n}^\mu(x) + \sum_n \left(-\frac{e^{A_s - \Phi}}{g_5} \partial_z \varphi_{a,n}(z) \right) \partial^\mu \hat{\pi}_{a,n}(x), \end{aligned} \quad (\text{A.19})$$

On the other hand, the meson decay constant are defined by the following relations

$$\begin{aligned} \langle 0 | J_{V,a}^\mu(x) | V^{b,m}(p, \lambda) \rangle &= F_{v^{a,m}} e^{-ip \cdot x} \epsilon^\mu(p, \lambda) \delta^{ab}, \\ \langle 0 | J_{A,a}^\mu(x) | A^{b,m}(p, \lambda) \rangle &= F_{a^{a,m}} e^{-ip \cdot x} \epsilon^\mu(p, \lambda) \delta^{ab}, \\ \langle 0 | J_{A,a}^\mu(x) | \pi^{b,m}(p) \rangle &= f_{\pi^{a,m}} e^{-ip \cdot x} \delta^{ab}, \end{aligned} \quad (\text{A.20})$$

The quantities $F_{v,a,m}$, $F_{a^a,m}$, $f_{\pi^a,m}$ are the decay constant of the vector, axial-vector and pseudoscalar mesons. Comparing (A.19) and (A.20) we arrive at the holographic dictionary for meson decay constants

$$\begin{aligned} F_{v_{a,n}} &= -\frac{e^{A_s-\Phi}}{g_5} \partial_z v_{a,n}(z), & F_{a_{a,n}} &= -\frac{e^{A_s-\Phi}}{g_5} \partial_z a_{a,n}(z) \\ f_{\pi_{a,n}} &= -\frac{e^{A_s-\Phi}}{g_5} \partial_z \varphi_{a,n}(z). \end{aligned} \quad (\text{A.21})$$

B The GKK model: A review

In this section we summarize the model investigated in Ref. [11], known as the Gherghetta-Kapusta-Kelley (GKK) model. This model was motivated by the original soft wall model [1], which considers a quadratic dilaton from the UV to the IR. In turn, the GKK model proposes to determine the dilaton, which is determined by solving the differential equation

$$\partial_z \Phi(z) = \frac{\partial_z^2 v}{\partial_z v} - e^{2A_s(z)} \left(m_X^2 - \frac{\kappa}{2} v^2 \right) \frac{v}{\partial_z v} + 3\partial_z A_s(z). \quad (\text{B.1})$$

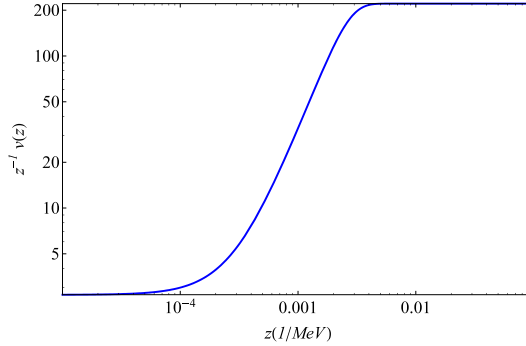


Figure 26. Profile of the tachyon, to get this figure we fix the parameters: $\kappa = 15$, $m_q = 9.75 \text{ MeV}$, $\Sigma = (204.5 \text{ MeV})^3$ and $\phi_\infty = 0.1831 \text{ GeV}^2$.

We observe that this equation depends on the tachyon field. thus, to solve this equation we must know the tachyon. On the other hand, the asymptotic expansion of the tachyon field close to the boundary takes the form $v = c_1 z + c_3 z^3$. In turn, in the IR the tachyon is linearly divergent, $v \sim z$. Additional constraints were imposed by the phenomenology, see Ref. [11] for details. Thus, the following interpolation function recovers the asymptotic behavior in the UV and IR

$$v(z) = z \left(A + B \tanh(Cz^2) \right), \quad (\text{B.2})$$

where the parameters of the model are defined as

$$A = \frac{\sqrt{N_c} m_q}{2\pi}, \quad B = 2\sqrt{\frac{\phi_\infty}{\kappa}} - \frac{\sqrt{N_c} m_q}{2\pi}, \quad C = \frac{2\pi\Sigma}{\sqrt{N_c} B}. \quad (\text{B.3})$$

Close to the UV (B.2) takes the form

$$v(z) = A z + B C z^3 + \dots, \quad (\text{B.4})$$

where $A \propto m_q$ and $BC \propto \Sigma$. In the way the parameters were defined in Eq. (B.3), we can see that in the chiral limit, i.e., $m_q \rightarrow 0$, $\Sigma \neq 0$, which means the spontaneous chiral symmetry breaking is nonzero. In the IR the tachyon reduces to

$$v(z) = (A + B)z = 2\sqrt{\frac{\phi_\infty}{\kappa}}z. \quad (\text{B.5})$$

A plot of the tachyon field is shown in Fig. 26. In turn, the dilaton field and its derivative are displayed in the left and right panels of Fig. 27, respectively. As we can see, we notice that the dilaton field becomes negative in a small region close to the boundary. However, regarding the analysis developed in Ref. [38], a negative dilaton violates the null energy condition in the gravitational side, where the dilaton must rise monotonically so that $\Phi'(z) > 0$.¹ Hence, maybe this pathological behavior will have consequences in the spectrum.

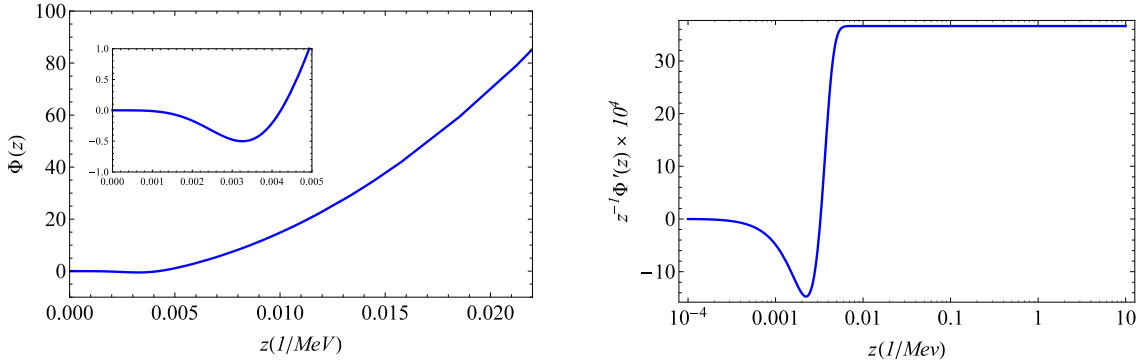


Figure 27. Left: profile of the dilaton field. Right: profile of the derivative of the dilaton. Both results were obtained setting $\kappa = 15$, $m_q = 9.75\text{MeV}$, $\Sigma = (404.5\text{MeV})^3$ and $\phi_\infty = 0.1831\text{GeV}^2$.

B.1 Scalar sector

We have a special interest in the spectrum of the scalar sector of this model. Then, let us compute the spectrum. For doing that we must rewrite the perturbation equation in the Schrödinger form and solve it using a shooting method, for example. A plot of the potential is shown in the left panel of Fig. 28. The results of the spectrum are displayed in the first column of Table 12, where we see that the first state has

¹It is worth mentioning that the analysis done by Kiritsis and Nitti in Ref. [38] states that the dilaton field should be monotonically increasing. However, as the soft wall model is not backreacted maybe the null energy condition can be “relaxed” in some kind at least locally.

an imaginary mass, which means an instability, i.e., $m_s^2 < 0$. It is worth mentioning that this instability was reported previously in Ref. [33] (see also [40]). To guarantee that this state is, in fact, a solution of the Schrödinger equation, we plot the wave functions of the corresponding first fourth eigenvalues in the right panel of Fig. 28. All these results were obtained using the same parameters used in Ref. [11].

n	Model	GKK [11]	f_0 experimental [20]
1	748 i	799	550^{+250}_{-150}
2	799	1184	980 ± 10
3	1184	1466	1350 ± 150
4	1465	1699	1505 ± 6
5	1698	1903	1724 ± 7
6	1902	2087	1992 ± 16
7	2087	2257	2103 ± 8
8	2256	2414	2314 ± 25

Table 12. The masses (in MeV) obtained in the modified version of the soft wall model, including quartic interaction term, compared against the results of [11] and experimental results of RPP [20]. The value of the parameters used are: $\kappa = 15$, $m_q = 9.75\text{MeV}$, $\Sigma = (404.5\text{MeV})^3$ and $\phi_\infty = 0.1831\text{GeV}^2$.

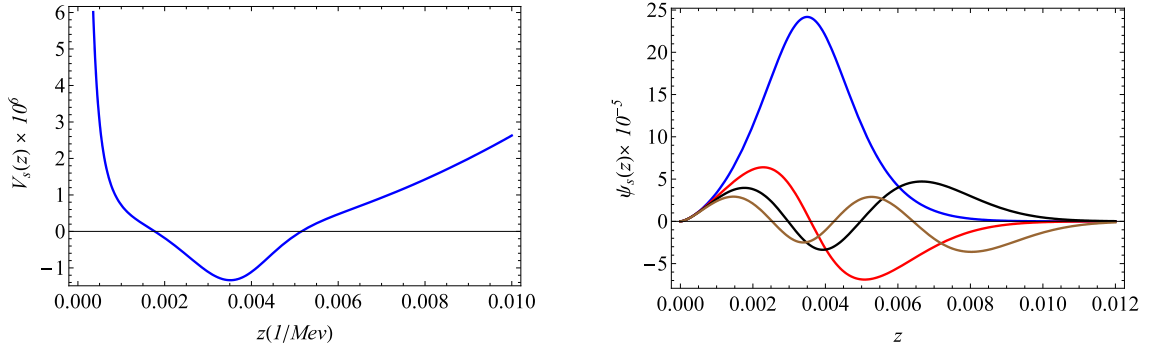


Figure 28. Left: potential of the Schrödinger equation associated with the scalar mesons. Right: first fourth wave functions associated with the scalar mesons, see Table 12. Both results were obtained setting $\kappa = 15$, $m_q = 9.75\text{MeV}$, $\Sigma = (204.5\text{MeV})^3$ and $\phi_\infty = 0.1831\text{GeV}^2$.

C Numerical analysis: nonlinear soft wall model

Here we write some details of our numerical results obtained investigating the tachyon field in the model for $\lambda < 0$. We fix the parameter $\phi_\infty = (388\text{MeV})^2$. Then, we solve

the differential equation (3.3) numerically, considering a family of two parametric solutions in the UV and a family of one parametric solution in the IR. We use as boundary condition the asymptotic solution in the IR (3.9). In the following analysis, we focus in the energy scale in the UV, such that the energy belongs to the interval $[10^3, 10^6]\text{MeV}$, which is equivalent to the interval of the holographic coordinate $z \in [10^{-6}, 10^{-3}]\text{MeV}^{-1}$, which lies close to the boundary. Thus, the problem was reduced to solve a one parameter family of solutions in the IR and two parameter family of solutions in the UV. What is expected is a non-trivial relationship between these parameters, which is obtained solving numerically Eq. (3.3). Our numerical results for c_3 as a function of c_1 are displayed in Fig. 29 for different values of λ . From this figure, we observe that besides the trivial solution there are solutions with $c_3 \neq 0$ in the chiral limit, i.e., $c_1 \rightarrow 0$, which corresponds to the limit of spontaneous chiral symmetry breaking.

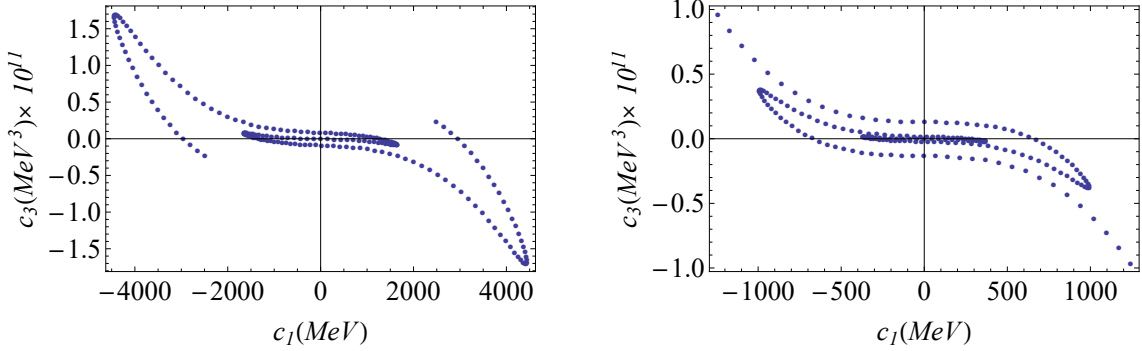


Figure 29. Numerical results of the nonlinear soft wall model. The corresponding parameters are: $\lambda = -1$ (left panel) and $\lambda = -20$ (right panel).

We point out that from the set of solutions showed in Fig. 29, the physical solutions are those for what the tachyon field is a monotonic increasing function. The corresponding solutions for c_1 as a function of C_0 are displayed in Fig. 30, whereas c_3 as a function of C_0 are displayed in Fig. 31. However, when computing the spectrum of the vector mesons, for example, we obtain an inconsistency arising when we calculate the potential of the Schrödinger equation, which is given by

$$V_V = \frac{15}{4z^2} + \phi_\infty^2 z^2 + 2\phi_\infty. \quad (\text{C.1})$$

At $z_{\min} = 10^{-6}\text{MeV}^{-1}$, the first term of the last equation is leading, such that $V_V \sim (10^{10}\text{MeV})^2$. On the other hand, at $z_{\max} = 10^{-3}\text{MeV}^{-1}$, the first term is still the leading $V_V \sim (10^3\text{MeV})^2$, meaning that the potential is a monotonic decreasing function with no potential well. We also realized that the convergence of the asymptotic solution (3.9) is not guaranteed.

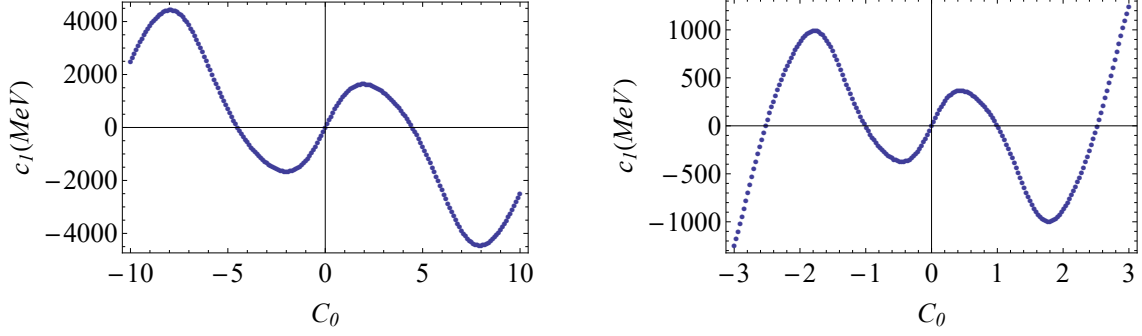


Figure 30. Numerical results of the nonlinear soft wall model. The corresponding parameters are: $\lambda = -1$ (left panel) and $\lambda = -20$ (right panel).

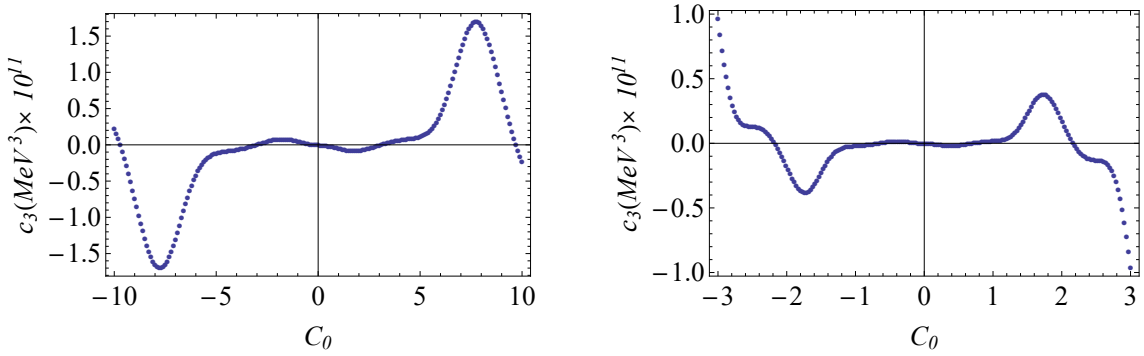


Figure 31. Numerical results of the nonlinear soft wall model. The corresponding parameters are: $\lambda = -1$ (left panel) and $\lambda = -20$ (right panel).

In conclusion, the above analysis shows us that there is spontaneous chiral symmetry breaking in the nonlinear soft wall model for $\lambda < 0$. However, it is arising in the UV. This conclusion may be justified because of the confinement scale introduced by the dilaton field is “fake”, because the dilaton is introduced by hand and the backreaction on the metric neglected.

References

- [1] A. Karch, E. Katz, D. T. Son and M. A. Stephanov, Phys. Rev. D **74**, 015005 (2006). [hep-ph/0602229].
- [2] S. R. Coleman and E. Witten, Phys. Rev. Lett. **45**, 100 (1980).
- [3] Y. Kinar, E. Schreiber and J. Sonnenschein, Nucl. Phys. B **566**, 103 (2000) [hep-th/9811192].
- [4] J. M. Maldacena, Phys. Rev. Lett. **80**, 4859 (1998) [hep-th/9803002].
- [5] J. Erlich, E. Katz, D. T. Son and M. A. Stephanov, Phys. Rev. Lett. **95**, 261602 (2005). [hep-ph/0501128].

- [6] L. Da Rold and A. Pomarol, Nucl. Phys. B **721**, 79 (2005) [hep-ph/0501218].
- [7] J. Polchinski and M. J. Strassler, Phys. Rev. Lett. **88**, 031601 (2002) [hep-th/0109174].
- [8] C. McNeile, A. Bazavov, C. T. H. Davies, R. J. Dowdall, K. Hornbostel, G. P. Lepage and H. D. Trottier, Phys. Rev. D **87**, no. 3, 034503 (2013) [arXiv:1211.6577 [hep-lat]].
- [9] K. Chelabi, Z. Fang, M. Huang, D. Li and Y. L. Wu, JHEP **1604**, 036 (2016) [arXiv:1512.06493 [hep-ph]].
- [10] I. Iatrakis, E. Kiritsis and A. Paredes, JHEP **1011**, 123 (2010). [arXiv:1010.1364 [hep-ph]].
- [11] T. Gherghetta, J. I. Kapusta and T. M. Kelley, Phys. Rev. D **79**, 076003 (2009). [arXiv:0902.1998 [hep-ph]].
- [12] H. Boschi-Filho and N. R. F. Braga, JHEP **0305**, 009 (2003) [hep-th/0212207].
- [13] A. Cherman, T. D. Cohen and E. S. Werbos, Phys. Rev. C **79**, 045203 (2009). [arXiv:0804.1096 [hep-ph]].
- [14] C. Csaki and M. Reece, JHEP **0705**, 062 (2007) doi:10.1088/1126-6708/2007/05/062 [hep-ph/0608266].
- [15] U. Gursoy, E. Kiritsis and F. Nitti, JHEP **0802**, 019 (2008). [arXiv:0707.1349 [hep-th]].
- [16] A. Ballon-Bayona, H. Boschi-Filho, L. A. H. Mamani, A. S. Miranda and V. T. Zanchin, Phys. Rev. D **97**, no. 4, 046001 (2018) [arXiv:1708.08968 [hep-th]].
- [17] P. Colangelo, F. De Fazio, F. Giannuzzi, F. Jugeau and S. Nicotri, Phys. Rev. D **78**, 055009 (2008) [arXiv:0807.1054 [hep-ph]].
- [18] A. Karch, A. O'Bannon and K. Skenderis, JHEP **0604**, 015 (2006) [hep-th/0512125].
- [19] C. P. Herzog, Phys. Rev. Lett. **98**, 091601 (2007). [hep-th/0608151].
- [20] M. Tanabashi *et al.* [Particle Data Group], Phys. Rev. D **98**, no. 3, 030001 (2018).
- [21] L. Da Rold and A. Pomarol, JHEP **0601**, 157 (2006). [hep-ph/0510268].
- [22] A. Ballon-Bayona, G. Krein and C. Miller, Phys. Rev. D **91** (2015) 065024. [arXiv:1412.7505 [hep-ph]].
- [23] T. M. Kelley, S. P. Bartz and J. I. Kapusta, Phys. Rev. D **83** (2011) 016002. [arXiv:1009.3009 [hep-ph]].
- [24] A. Ballon-Bayona, G. Krein and C. Miller, Phys. Rev. D **96**, no. 1, 014017 (2017). [arXiv:1702.08417 [hep-ph]].
- [25] H. J. Kwee and R. F. Lebed, JHEP **0801**, 027 (2008). [arXiv:0708.4054 [hep-ph]].
- [26] H. J. Kwee and R. F. Lebed, Phys. Rev. D **77**, 115007 (2008). [arXiv:0712.1811 [hep-ph]].

- [27] A. Holl, A. Krassnigg and C. D. Roberts, Phys. Rev. C **70**, 042203 (2004).
[nucl-th/0406030].
- [28] A. Krassnigg, C. D. Roberts and S. V. Wright, Int. J. Mod. Phys. A **22**, 424 (2007).
- [29] P. Maris and P. C. Tandy, Nucl. Phys. Proc. Suppl. **161**, 136 (2006).
[nucl-th/0511017].
- [30] Z. Fang, Y. L. Wu and L. Zhang, Phys. Lett. B **762**, 86 (2016). [arXiv:1604.02571 [hep-ph]].
- [31] A. Vega and I. Schmidt, Phys. Rev. D **82**, 115023 (2010). [arXiv:1005.3000 [hep-ph]].
- [32] M. Jarvinen and E. Kiritsis, JHEP **1203**, 002 (2012) [arXiv:1112.1261 [hep-ph]].
- [33] Y. Q. Sui, Y. L. Wu, Z. F. Xie and Y. B. Yang, Phys. Rev. D **81** (2010) 014024.
[arXiv:0909.3887 [hep-ph]].
- [34] I. Iatrakis, E. Kiritsis and A. Paredes, Phys. Rev. D **81**, 115004 (2010)
[arXiv:1003.2377 [hep-ph]].
- [35] R. Casero, E. Kiritsis and A. Paredes, Nucl. Phys. B **787**, 98 (2007).
[hep-th/0702155 [HEP-TH]].
- [36] L. X. Cui, Z. Fang and Y. L. Wu, Eur. Phys. J. C **76**, no. 1, 22 (2016).
- [37] A. Karch, E. Katz, D. T. Son and M. A. Stephanov, JHEP **1104**, 066 (2011)
[arXiv:1012.4813 [hep-ph]].
- [38] E. Kiritsis and F. Nitti, Nucl. Phys. B **772**, 67 (2007). [hep-th/0611344].
- [39] Z. Abidin and C. E. Carlson, Phys. Rev. D **80**, 115010 (2009). [arXiv:0908.2452 [hep-ph]].
- [40] D. Li and M. Huang, JHEP **1311**, 088 (2013). [arXiv:1303.6929 [hep-ph]].